DESIGN AND IMPLEMENTATION OF A FIXED-FREQUENCY INDUCTIVE POWER TRANSFER SYSTEM

Bernardo Peschiera

A Thesis

in

The Department

of

Electrical and Computer Engineering

Presented in Partial Fulfillment of the Requirements

for the Degree of Master of Applied Science at

Concordia University

Montréal, Québec, Canada

April 2014

CONCORDIA UNIVERSITY
School of Graduate Studies

This is to certify that the Thesis prepared

By: Bernardo Peschiera I.D. 6080073

Entitled: "Design and Implementation of a Fixed-frequency Inductive Power Transfer System"

and submitted in partial fulfillment of the requirements for the degree of

Master of Applied Science

complies with the regulations of the University and meets the accepted standards with respect to originality and quality.

Signed by the final examining committee:

_____ Chair
Dr. M. Z. Kabir

_____ External Examiner
Dr. S. Narayanswamy (MIE)

_____ Examiner
Dr. L. A. Lopes

_____ Supervisor
Dr. S. Williamson

Approved by _____
Dr. William E. Lynch
Chair, Department of Electrical and Computer Engineering

_____
Dr. Christopher W. Truemam
Dean, Faculty of Engineering and Computer Science

Date _____

ABSTRACT

Design and Implementation of a Fixed-frequency Inductive Power Transfer System

Bernardo Peschiera

Inductive power tranfer (IPT) technology has gained immense interest for battery charging applications. IPT proves to be particularly efficient and suitable for high-power applications (≈1-20kW) . This makes IPT an effective alternative for charging large batteries of electric vehicles (EVs), especially large electric transit vehicles, such as trains, trams, and buses.

Because of the trend that this technology is having, it is important to understand the general characteristics and its applications. Nowadays, it is not a secret that IPT technology is and will continue revolutionizing the industry and our society. The future vision is to change the way electricity has been observed since its discovery: through wires.

The main objective of this thesis is to study in details the fundamentals of IPT technology and analyze two principal stages of the system: the power supply and the resonant circuit, in order to design an IPT system using effective techniques, which will improve its performance. Additionally, the thesis helps identify and suggest a design procedure that can benefit and motivate future work on this technology. Moreover, the thesis presents a prototype setup that was built in the laboratory, in order to validate the theoretical analysis and simulation results.

The thesis is structured into four main parts; the first part reviews the concepts of IPT systems, the different topologies, the explanation of important design considerations, and finally, presents initial simulation results. The second part explains the characteristics of the power supply in IPT systems, the control techniques to regulate the power flow, the explanation of a proposed control strategy, and the simulation results. The third part presents the experimental test setup and related results. Finally, the fourth part presents the conclusions and suggested future work.

ACKNOWLEDGMENTS

The author would like to express his most sincere gratitude to his supervisor, Prof. Sheldon S. Williamson, for his patient and invaluable guidance, advice, and friendship throughout the author's Master's program. Also, the author deeply appreciates the financial support from his supervisor. The author also would like to thank the other professors and colleagues in the Power Electronics and Energy Research Group, at the P. D. Ziogas Power Electronics Laboratory.

Last, but not least, the author would like to extend his sincere gratitude to his family and wife, Alexandra Suarez. Alexandra's patience, understanding, and unconditional support were key factors throughout this journey.

To my wife and my parents

Table of Contents

LIST OF FIGURES

LIST OF TABLES

LIST OF ACRONYMS

AC	Alternating Current
ADC	Asymmetrical Duty Cycle
AGV	Automated Guided Vehicles
AVC	Asymmetrical Voltage Cancelation
CPTT	Contactless Power Transfer Transformer
DC	Direct Current
EVs	Electric Vehicles
FFT	Fast Fourier Transform
Hz	Hertz
IPT	Inductive Power Transfer
IPTT	Inductive Power Transfer Transformer
LCR	Inductor Capacitor Resistance connection
o_AVC	Optimum Asymmetrical Voltage Cancelation
PF	Power Factor
PP	Parallel-Parallel topology
PS	Parallel-Series topology
PWM	Pulse-Width Modulation
SN	Served with nylon textile
SP	Series-Parallel topology
SPN	Single build Polyurethane-Nylon
SS	Series-Series topology

THD	Total Harmonic Distortion
VA	Volt-Ampere
WPT	Wireless Power Transfer
WPTT	Wireless Power Transfer Transformer
ZPA	Zero Phase Angle
ZVS	Zero Voltage Switching

LIST OF PRINCIPAL SYMBOLS

C_1	Primary Capacitor
C_2	Secondary Capacitor
I_{sc}	Short Circuit Current
L_1	Primary Self Inductance
L_2	Secondary Self Inductance
L_a	Primary Leakage Inductance
L_b	Secondary Leakage Inductance
Q_1	Primary Loaded Quality Factor
Q_2	Secondary Loaded Quality Factor
R_1	Primary Coil Resistance
R_2	Secondary Coil Resistance
R_{ac}	Resistive Load
$V_{1(1)}$	Fundamental Component of Primary Voltage
V_1	Primary Voltage
V_2	Secondary Voltage
V_{dc}	DC Link Voltage
V_{oc}	Open Circuit Voltage
Z_R	Reflected Impedance
Z_{eq}	Equivalent Impedance

f_o	Resonant Frequency
f_s	Switching Frequency
ω_o	Resonant Angular Frequency
ω_s	Switching Angular Frequency
ϕ_1	Primary Leakage Flux
ϕ_2	Secondary Leakage Flux
ϕ_m	Mutual Flux
ϕ_{v1}	Primary Voltage Phase Shift
η	Efficiency
ImZ_{eq}	Equivalent Impedance Imaginary Component
M	Mutual Inductance
Z	Impedance
f	Frequency
k	Coupling Coefficient
$\Delta\phi$	Primary Voltage and Current Phase Shift
ω	Angular Frequency

CHAPTER 1

INTRODUCTION

1.1 Background

Over the last years, there have been important advances in power electronics. As a result, many research studies and ideas are now being positively impacted by these technological improvements. One example of this, is Inductive Power Transfer (IPT) technology, also known as "wireless" power transfer.

One of the reasons IPT technology has been gaining more interest is that it is safe, does not harm humans or animals, is waterproof, weatherproof and it has been proven to be very effective in charging electric vehicles (EVs) [1]-[2].

It is important to mention that IPT technology has been used for decades in electrical toothbrushes, and more recently in biomedical implants. However, this technology has been making strong advances for higher power applications (≈1-20kW). For example, charging cellular phones and EVs, supplying power to Automated Guided Vehicles (AGV) and electric transportation (buses and trains), and even supplying power to electronic devices like televisions, stereos, desktop computers, kitchen appliances, etc. Therefore, it is not a secret that this technology is and will continue revolutionizing the industry and our society.

The idea of transferring electricity through the air started in the 1900's with Nikola Tesla [36]. But it has never been considered so serious by companies and manufacturers until now, thanks to the technological advantages, especially in power electronics as it was mentioned before. Nowadays, companies like Witricity, Bombardier, Conductix, Evatran, Qualcomm and Siemens, are just a few that are working on wireless power transfer and IPT systems.

1.2 Inductive Power Transfer Systems

IPT technology can be defined as the effect of transferring power from a primary coil to a secondary coil through the air by inductive coupling and capacitive compensation. This arrangement will create a resonant circuit that increases the power transfer capabilities.

An IPT system can be represented by the following general block diagram, where each block or stage has a specific function in order to transfer power accordingly to design specifications.

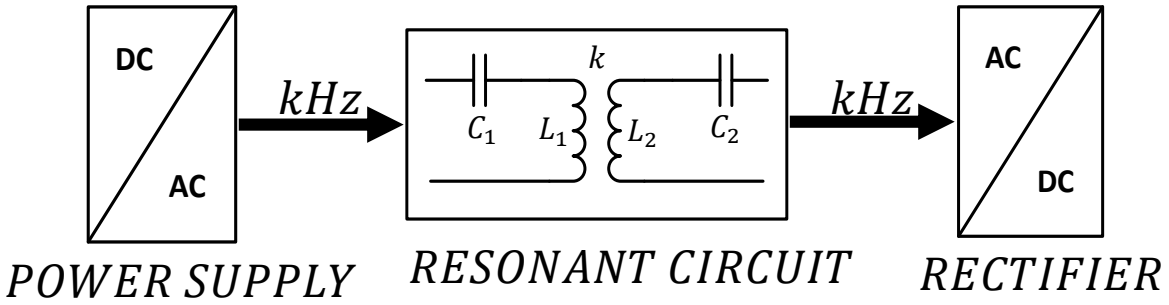

Fig. 1-1 General block diagram of an IPT system

It can be seen in the figure, that the system in composed by three blocks or stages: power supply, resonant circuit or resonant tank, and rectifier.

The power supply is normally constituted by an inverter which converts a DC current to an AC current in the kHz range. A primary and secondary coil connected to a primary and secondary capacitor will form the resonant circuit. This resonant condition will boost the power that can be transferred from the primary coil to the secondary coil. Here, the tuning conditions are essential for a good performance of the system. The primary coil can be identified as the transmitter and the secondary coil as the receiver. Finally, the power that is transferred to the secondary coil could be rectified to give a stable DC signal output.

The main purpose of this thesis is to study in detail the fundamentals of IPT technology and analyze its power supply and resonant circuit stages, in order to design and simulate an IPT system

using effective techniques to improve the performance to up to more than 85% of efficiency. Additionally, identify and propose a design procedure that can benefit and motivate future works on this technology.

1.3 Contribution of the Thesis

The mayor contributions of the thesis include:

(a) Proposing and using an optimal operation point strategy for the selection of an ideal switching frequency, based on the efficiency of the inductive power transfer transformer (IPTT).

(b) Identifying and implementing tuning and resonant considerations for the design of the IPTT.

(c) Identifying and validating with experimental results an optimum control strategy (o_AVC) for zero voltage switching (ZVS) operation, with fixed frequency control for series resonant inverters.

(d) Identifying and validating with experimental results a ZVS verification technique for resonant inverters.

(e) Designing and building a pulse generator for IPT applications, using dSpace and a SN7406 Hex Inverter.

(f) Designing and building a series-series compensated IPTT: primary and secondary coils, capacitive compensation circuit boards and a fixed resistive load.

1.4 Thesis Outline

The content of this thesis is organized into 5 chapters. Each chapter has the following general description:

Chapter 1 gives a general review on the background of IPT technology, its definition, and the different stages that represent an IPT system. Also, the major contributions of the thesis are presented.

Chapter 2 reviews the fundamentals of IPT technology, the type of topologies for capacitive compensation, and also explains the optimal operation point strategy that was identified as well as the tuning and resonant considerations. Finally, it shows the simulation results of the designed series-series compensated IPTT operating at resonant frequency.

Chapter 3 analyses the characteristics of the power supply for IPT systems, and also studies the different techniques of voltage regulation in the power supply stage for fixed frequency control. Additionally, explains the optimum control strategy (o_AVC) and the ZVS verification technique that were identified. Finally, it shows the simulation results of the designed IPT system operating with the optimum control strategy for voltage regulation.

Chapter 4 shows the construction procedure and tests results of the pulse generator setup and the series-series compensated IPTT with a fixed resistive load, validating theoretical design calculations with experiment results. Additionally, shows the practical results of the ZVS verification technique, also validating the analytical calculations. In addition, it also presents a user friendly interface display that was created for the pulse generator setup.

Chapter 5 summarizes the conclusions of this thesis and gives future research recommendations in order to give continuity to this work and to IPT technology studies in general.

CHAPTER 2

FUNDAMENTALS OF INDUCTIVE POWER TRANSFER TECHNOLOGY

2.1 Introduction

From the basics of electricity, to supply electrical energy to a load, this has to be connected to a source in order to receive this energy. Here, electrical power is being transferred through a physical connection between the source and the load. However, it is also possible to transfer electrical power from a source to a load with no physical connection between them. As it was mentioned before, one of the technologies used to accomplish this is IPT.

IPT was developed from the theory of electrical transformers [1]-[2]-[3]. An electrical transformer, transfers power from a primary coil to a secondary coil. This coils are wound around a common core to increase the coupling coefficient (k) between them. Normally, electrical transformers are used to increase or decrease the voltage from the primary side to the secondary side. But, because of the electrical isolation that exists between the primary coil and the secondary coil, they are also used for electrical protection. The source is isolated from the load, but at the same time they are magnetically coupled. This magnetic coupling is physically made by the common core. In typical electrical transformers, the coupling coefficient is ≈ 1.

Based on this, it is possible to remove the common core and achieve magnetic coupling between the primary coil and the secondary coil through the air. This modification leads to what has been called an IPT transformer (IPTT), contactless power transfer transformer (CPTT) or even wireless power transfer transformer (WPTT). In this way, electricity can be transferred "wirelessly". This idea of transferring electricity through the air is not new, it started in the 1900's

with Nikola Tesla. A representation of how the different fluxes behave in an IPTT is represented in the following figure.

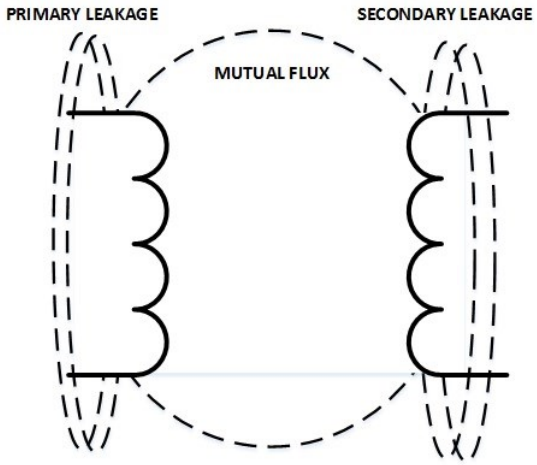

Fig. 2-1 Leakage and mutual flux in an IPTT

It can be seen that the primary leakage, is the flux that is generated in the primary coil that does not link with the secondary coil; this is called primary leakage flux (ϕ_1). A secondary leakage flux (ϕ_2) is also generated. The mutual flux (ϕ_m), is the flux that links both sides in the IPTT. These fluxes can be electrically represented as inductances [4]. Therefore, they are described as primary leakage inductance (L_a), secondary leakage inductance (L_b) and mutual inductance (M).

Because of the large air gap in an IPTT, the leakage flux in the primary and secondary side is very high, consequently, increasing the leakage inductances and decreasing the mutual inductance. Therefore, the coupling coefficient is affected to a point where it becomes weak or very small. Logically, the power transfer capability is enormously affected.

However, the power transfer capability could be improved by connecting two capacitors; one in the primary side and the other one in the secondary side [3]-[5]-[6]. This arrangement will generate a capacitive compensation that will boost the power to be transferred. This effect will be explained more in details in the next sections of this chapter.

In practice, IPT systems can be implemented in home applications, by supplying power to appliances or electronic devices. Also, in transportation applications, by charging EVs and supplying power to electrified railways or people movers. And moreover, in the industry, by supplying power to automatic guided vehicles (AGV) [7]. It is important to mention that in any application where IPT technology is implemented, the primary coil serves as the transmitter and the secondary coil as the receiver [44].

2.2 Inductive Power Transfer Transformer Coupling Model

From what was mentioned before, and IPTT is composed by a primary coil and a secondary coil, which are separated by an air gap. In order to analyze the behavior of the system, an equivalent circuit needs to be modeled. Each component can be identified as follows. The primary coil can be represented by a winding resistance (R_1) in series with the self-inductance (L_1). In the same way, the secondary coil could be represented by a winding resistance (R_2) in series with the self-inductance (L_2). As it was mentioned in the previous section, because of the air gap, the mutual inductance (M) becomes an important factor in the analysis of the IPTT. A relation between M and the coupling coefficient (k) is well known to be:

$$M = k\sqrt{L_1 L_2} \tag{1}$$

The IPTT can be modeled from the theory of inductive coupling. Assuming sinusoidal voltages and currents, the voltage induced in the secondary coil due to the current in the primary coil is equal to $j\omega M I_1$. In the same way, the voltage reflected in the primary coil due to the current in the secondary coil is equal to $-j\omega M I_2$, where ω is the operational frequency. This explanation is represented in the following figure [8].

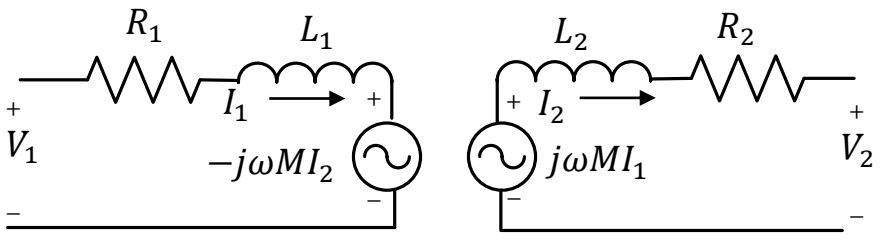

Fig. 2-2 IPTT coupling model

The coupling model shown in figure 2-2, represents how the primary side is induced in the secondary side and how the secondary side is reflected to the primary side. The equivalent secondary impedance reflected to the primary side is determined by the following equation [3].

$$Z_R = \frac{\omega^2 M^2}{Z_2} \tag{2}$$

Equation 2 is derived as follows. From figure 2-2, it can be seen that:

$$I_2 = \frac{j\omega I_1}{Z_2} \tag{3}$$

The voltage reflected in the primary side can be calculated as follows:

$$V_1{}' = -j\omega MI_2 \tag{4}$$

Substituting equation 3 in equation 4, and after doing some mathematical simplifications, the final equation is obtained, which is equal to equation 2.

$$\frac{V_1{}'}{I_1} = \frac{\omega^2 M^2}{Z_2} \tag{5}$$

Equation 5 represents the load effect of the secondary side reflected to the primary side. The next figure shows how it could be represented graphically.

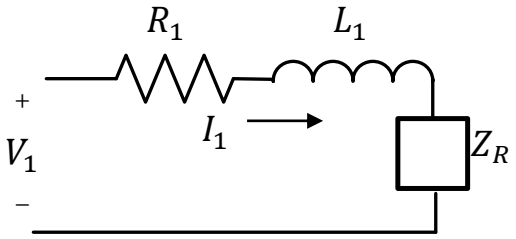

Fig. 2-3 Equivalent secondary impedance reflected to the primary side

From figure 2-3 and equation 2, the resulting equivalent impedance of an IPTT is defined by the following equation.

$$Z_{eq} = R_1 + j\omega L_1 + \left[\frac{\omega^2 M^2}{R_2 + R_{ac} + j\omega L_2}\right] \tag{6}$$

When an IPTT is magnetically coupled; the self-inductance of the primary coil (L_1) is equivalent to $L_a + M$ and the self-inductance of the secondary coil (L_2) is equivalent to $L_b + M$ [4]-[9]-[10]. Therefore, equation 6 can also be represented as follows.

$$Z_{eq} = R_1 + j\omega(L_a + M) + \left[\frac{\omega^2 M^2}{R_2 + R_{ac} + j\omega(L_b + M)}\right] \tag{7}$$

This final equation leads to the equivalent circuit for an IPTT. Figure 2-4 shows the circuit, where V_1 is a sinusoidal voltage source, I_1 is the current in the primary coil, I_2 is the current in the secondary coil, V_2 is the voltage in the output of the IPTT and R_{ac} a resistive load. This approach facilitates the analysis of the system [9]-[10].

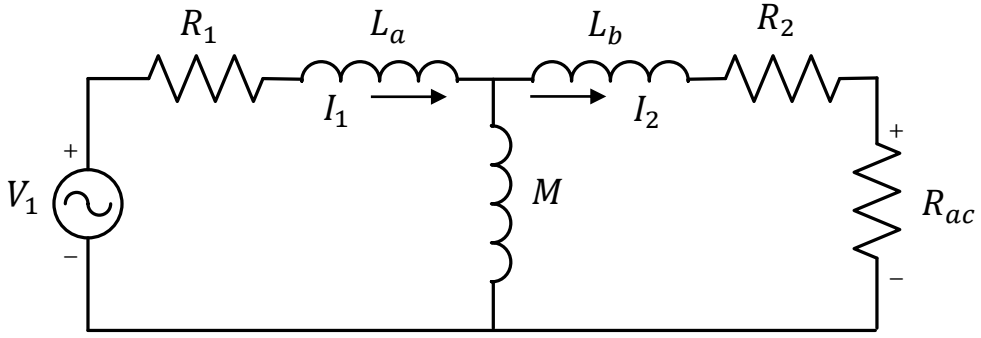

Fig. 2-4 Equivalent circuit of an IPTT

2.3 Capacitive Compensation

Based on the equivalent circuit shown in figure 2-4, the behavior of an IPTT can be studied more easily. In this section, the impact of the Z_{eq} over the power transfer capability and how this problem could be resolved by capacitive compensation will be discussed.

It can be seen in equation 7, that the equivalent impedance of an IPTT has an inductive load characteristic. But unfortunately, the more inductive Z_{eq} is; the less capable in transferring power the system will become. This is because the system will have a low power factor. Based in all the concepts that have been reviewed so far, it is possible to make the following general analysis: the larger the air gap in the IPT transformer, the larger will be the leakage-flux and leakage-inductance; therefore, the system will become more inductive and consequently the power factor will decrease affecting the power transfer capability of the system.

However, like it was mentioned before, the power transfer capability could be improved by connecting two capacitors; one in the primary side (C_1) and the other one in the secondary side (C_2). This arrangement will generate a capacitive compensation that will boost the power to be transferred. This technique is called capacitive compensation.

This method is implemented to compensate the power factor to a point where Z_{eq} becomes purely resistive. Therefore, the power transfer capability is maximized to a unity power factor [9]-[11]. However, this condition only occurs at a specific operational frequency (ω) called resonant frequency (ω_o).

The capacitor in the secondary side, referred as secondary compensation, improves the power transferred to the load, while the capacitor in the primary side, referred as primary compensation, will decrease the VA ratings by achieving unity power factor. This is because the primary

capacitance compensates the total reflected inductance of the circuit, forcing the zero phase angle (ZPA) [12]-[13].

There are four different types of compensation topologies that can be used in an IPTT: series-series (SS), series-parallel (SP), parallel-series (PS) and parallel-parallel (PP) [3]-[6]-[11]. The following figure shows the topologies.

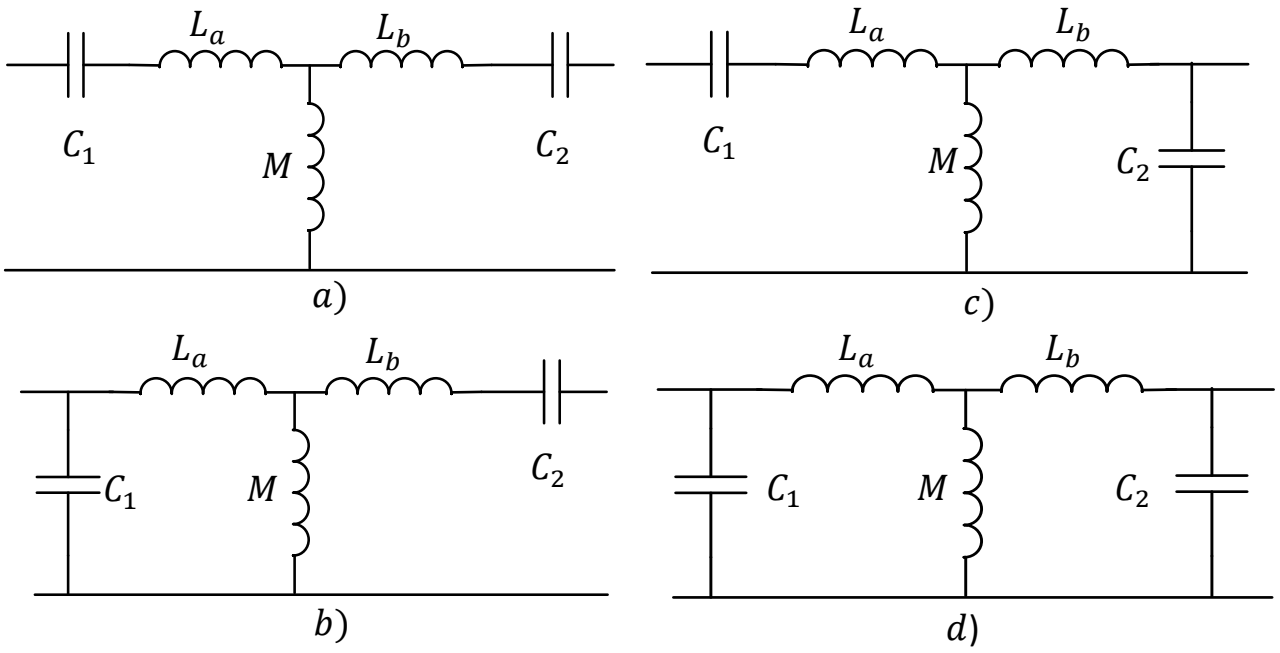

Fig. 2-5 Capacitive compensation topologies in a IPTT

For the capacitive compensation design, it is important to follow a procedure. The first step is to calculate the value of the capacitor for the secondary compensation (C_2). From resonance theory, the secondary compensation will be established under the condition of equation 8 and resulting in equation 9.

$$j\omega_o L_2 - \frac{j}{\omega_o C_2} = 0 \tag{8}$$

$$C_2 = \frac{1}{{\omega_o}^2 L_2} \tag{9}$$

It can be seen in the previous equations, that resonant frequency (ω_o) is being used. This is because, like it was mentioned before, at that frequency the power transfer capability is maximized to a unity power factor.

Until this point, the value of the secondary capacitance to achieve resonant conditions can be calculated by using equation 9.

The value of the capacitor for primary compensation (C_1) will depend on the type of topology used. As it was mentioned before, the primary compensation minimizes the VA ratings of the power supply. The ideal condition is to achieve zero phase angle (PF=1). This means that the primary compensation is designed in such a way that the primary capacitance resonates with the total reflected impedance of the circuit, forcing the zero phase angle (ZPA). As it was reviewed previously, a total of four topologies can be used. In the next section, the equation to calculate the value of the capacitor for primary compensation is derived for each topology.

2.3.1 PRIMARY CAPACITIVE COMPENSATION IN A SERIES-SERIES TOPOLOGY

The equivalent circuit, for the SS capacitive compensation is shown in the following figure.

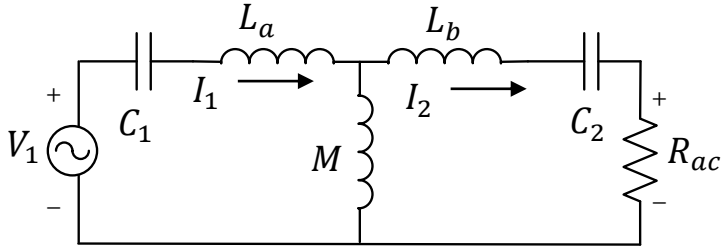

Fig. 2-6 Series-series capacitive compensation topology

The total equivalent impedance of the circuit can be determined as follows. The winding resistance is not considered to simplify the analysis.

$$Z_2 = j\omega L_2 + \frac{1}{j\omega C_2} + R_{ac} \tag{10}$$

$$Z_R = \frac{\omega^2 M^2}{j\omega L_2 + \frac{1}{j\omega C_2} + R_{ac}} \tag{11}$$

$$Z_{eq} = \frac{1}{j\omega C_1} + j\omega L_1 + \frac{\omega^2 M^2}{j\omega L_2 + \frac{1}{j\omega C_2} + R_{ac}} \tag{12}$$

It is known that ZPA is achieved when the imaginary part of Z_{eq} is equal to zero ($ImZ_{eq} = 0$) at resonant frequency. Therefore, using these two conditions in equation 12, the value of the capacitor for primary compensation in a SS topology can be calculated as follows.

$$C_1 = \frac{1}{\omega_o{}^2 L_1} \tag{13}$$

2.3.2 PRIMARY CAPACITIVE COMPENSATION IN A PARALLEL-SERIES TOPOLOGY

The equivalent circuit, for the PS capacitive compensation is shown in the following figure.

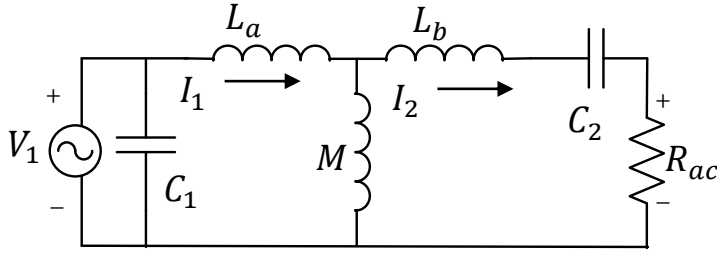

Fig. 2-7 Parallel-series capacitive compensation topology

Following the same approach as before, the total equivalent impedance of the circuit can be determined as follows. The winding resistance is not considered to simplify the analysis.

$$Z_2 = j\omega L_2 + \frac{1}{j\omega C_2} + R_{ac} \tag{14}$$

$$Z_R = \frac{\omega^2 M^2}{j\omega L_2 + \frac{1}{j\omega C_2} + R_{ac}} \tag{15}$$

$$Z_{eq} = \frac{1}{j\omega C_1 + \frac{1}{j\omega L_1 + \frac{\omega^2 M^2}{j\omega L_2 + \frac{1}{j\omega C_2} + R_{ac}}}} \tag{16}$$

In the same way as before, it is known that ZPA is achieved when the imaginary part of Z_{eq} is equal to zero ($ImZ_T = 0$) at resonant frequency. Therefore, using these two conditions in equation 16, the value of the capacitor for primary compensation in a PS topology can be calculated as follows.

$$C_1 = \frac{L_1}{\left(\frac{\omega_o{}^2 M^2}{R_{ac}}\right)^2 + \omega_o{}^2 L_1{}^2} \tag{17}$$

2.3.3 PRIMARY CAPACITIVE COMPENSATION IN A SERIES-PARALLEL TOPOLOGY

The equivalent circuit, for the SP capacitive compensation is shown in the following figure.

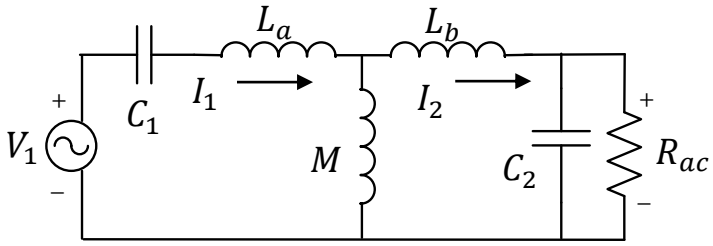

Fig. 2-8 Series-parallel capacitive compensation topology

Following the same approach as before, the total equivalent impedance of the circuit can be determined as follows. The winding resistance is not considered to simplify the analysis.

$$Z_2 = j\omega L_2 + \frac{R_{ac}}{j\omega C_2 R_{ac} + 1} \tag{18}$$

$$Z_R = \frac{\omega^2 M^2}{j\omega L_2 + \frac{R_L}{j\omega C_2 R_{ac} + 1}} \tag{19}$$

$$Z_{eq} = \frac{1}{j\omega C_1} + j\omega L_1 + \frac{\omega^2 M^2}{j\omega L_2 + \frac{R_L}{j\omega C_2 R_{ac}+1}} \tag{20}$$

In the same way as before, it is known that ZPA is achieved when the imaginary part of Z_{eq} is equal to zero ($ImZ_T = 0$) at resonant frequency. Therefore, using these two conditions in equation 20, the value of the capacitor for primary compensation in a SP topology can be calculated as follows.

$$C_1 = \frac{1}{\omega_o{}^2\left(L_1 - \frac{M^2}{L_2}\right)} \tag{21}$$

2.3.4 PRIMARY CAPACITIVE COMPENSATION IN A PARALLEL-PARALLEL TOPOLOGY

The equivalent circuit, for the PP capacitive compensation is shown in the following figure.

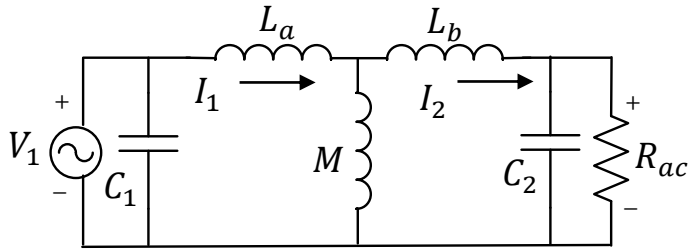

Fig. 2-9 Parallel-parallel capacitive compensation topology

Following the same approach as before, the total equivalent impedance of the circuit can be determined as follows. The winding resistance is not considered to simplify the analysis.

$$Z_2 = j\omega L_2 + \frac{R_{ac}}{j\omega C_2 R_{ac}+1} \tag{22}$$

$$Z_R = \frac{\omega^2 M^2}{j\omega L_2 + \frac{R_L}{j\omega C_2 R_{ac}+1}} \tag{23}$$

$$Z_{eq} = \frac{1}{j\omega C_1 + \frac{1}{j\omega L_1 + \frac{\omega^2 M^2}{j\omega L_2 + \frac{R_{ac}}{j\omega C_2 R_{ac} + 1}}}} \tag{24}$$

In the same way as before, it is known that ZPA is achieved when the imaginary part of Z_{eq} is equal to zero ($ImZ_T = 0$) at resonant frequency. Therefore, using these two conditions in equation 24, the value of the capacitor for primary compensation in a PP topology can be calculated as follows.

$$C_1 = \frac{L_1 - \frac{M^2}{L_2}}{\left(\omega_o L_1 - \frac{\omega_o M^2}{L_2}\right)^2 + \left(\frac{M^2 R_{ac}}{{L_2}^2}\right)^2} \tag{25}$$

2.4 Impedance Characteristics in Compensated Topologies

As it was reviewed previously, the equivalent impedance (Z_{eq}) will define the power transfer capability of the IPTT. Because capacitive elements have been added to the equivalent circuit, it is important to define the equivalent impedance for each topology and study the effect in each case.

The derivation of Z_{eq} for the four topologies is resumed in the following table.

Table 2-1 Equivalent Impedances for each topology

Topology	Equivalent Impedance
SS	$Z_{eq} = \frac{1}{j\omega C_1} + j\omega L_1 + \frac{\omega^2 M^2}{j\omega L_2 + \frac{1}{j\omega C_2} + R_{ac}}$
PS	$Z_{eq} = \frac{1}{j\omega C_1 + \frac{1}{j\omega L_1 + \frac{\omega^2 M^2}{j\omega L_2 + \frac{1}{j\omega C_2} + R_{ac}}}}$
SP	$Z_{eq} = \frac{1}{j\omega C_1} + j\omega L_1 + \frac{\omega^2 M^2}{j\omega L_2 + \frac{R_{ac}}{j\omega C_2 R_{ac} + 1}}$
PP	$Z_{eq} = \frac{1}{j\omega C_1 + \frac{1}{j\omega L_1 + \frac{\omega^2 M^2}{j\omega L_2 + \frac{R_{ac}}{j\omega C_2 R_{ac} + 1}}}}$

It can be seen that depending on the compensation topology, the equivalent impedance has a different expression. To show the behavior characteristics of Z_{eq} for each topology, an analysis was performed based on the parameters of the IPTT setup obtained in chapter 4. These values are shown in the following table.

Table 2-2 Parameters of the IPTT setup

Element	Value
L_1	149.03 µH
L_2	23.26 µH
M	13.115 µH
R_1	0.298 Ω
R_2	0.1175 Ω
k	0.223
Air Gap	25 mm
f	40 kHz

The load will be fixed at $R_{ac} = 1.3\ \Omega$. Using equations 9, 13, 17, 21 and 25 the resulting theoretical values of the capacitors for each topology is shown in the following table:

Table 2-3 Values of the capacitors for each topology for impedance analysis

Element	Value
C_2	680.63 nF
C_1(SS)	106.23 nF
C_1(PS)	101.2 nF
C_1(SP)	111.77 nF
C_1(PP)	111.76 nF

For these values, the curve characteristic of Z_{eq} for each topology are shown in the following figures.

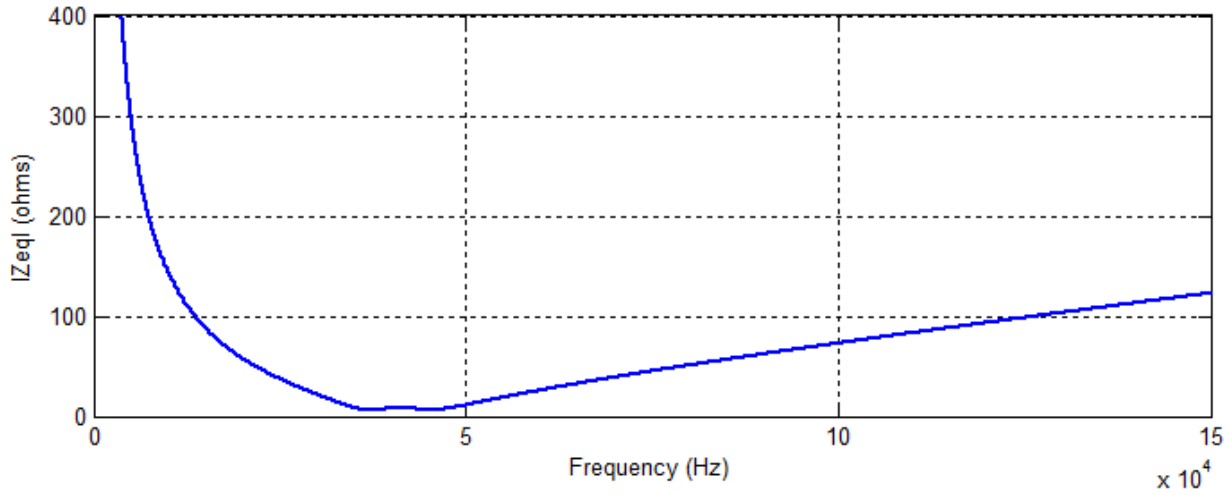

Fig. 2-10 Impedance characteristic in SS topology

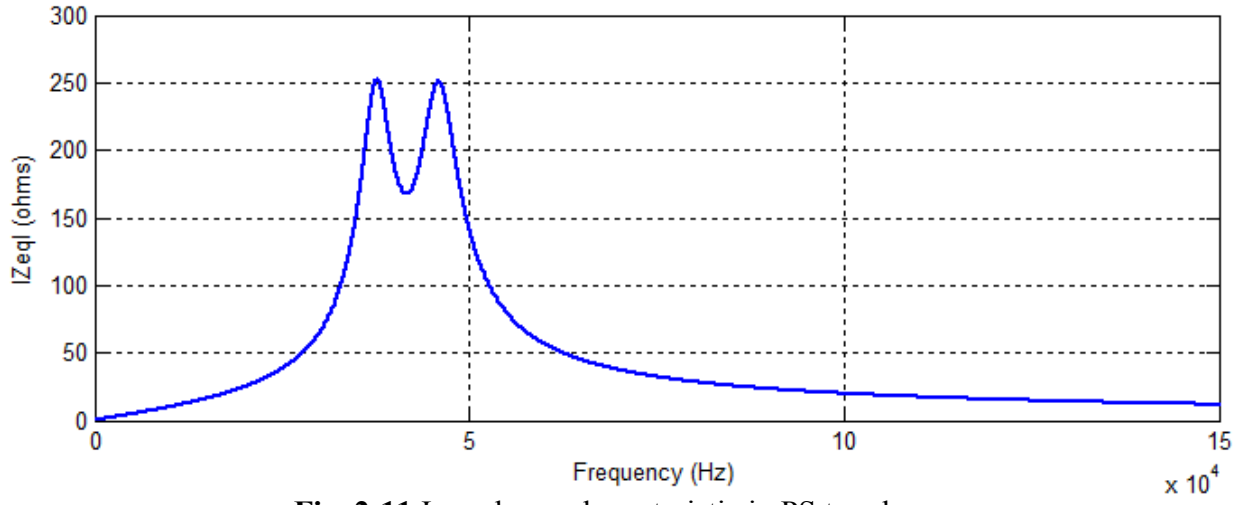

Fig. 2-11 Impedance characteristic in PS topology

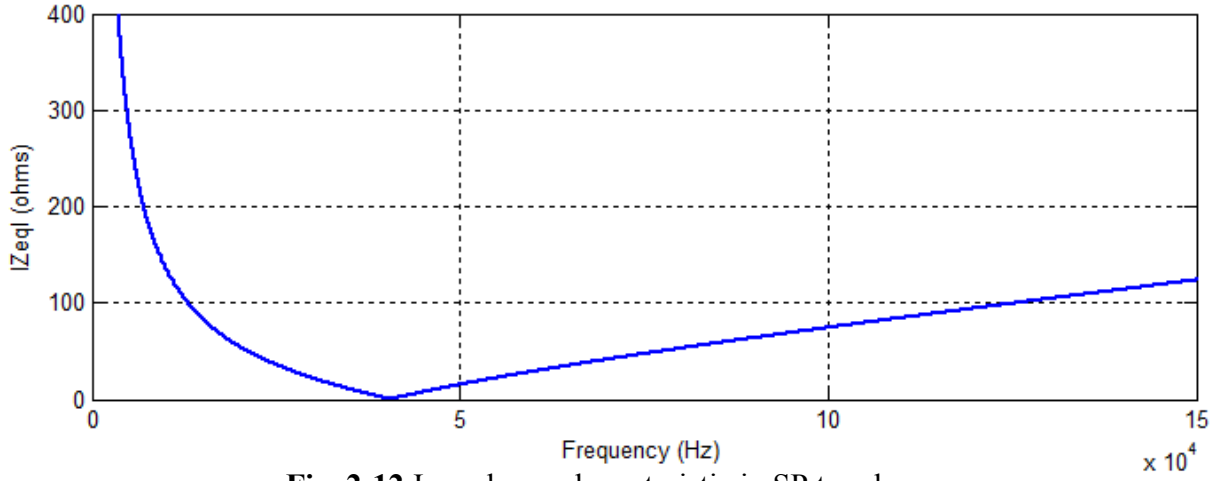

Fig. 2-12 Impedance characteristic in SP topology

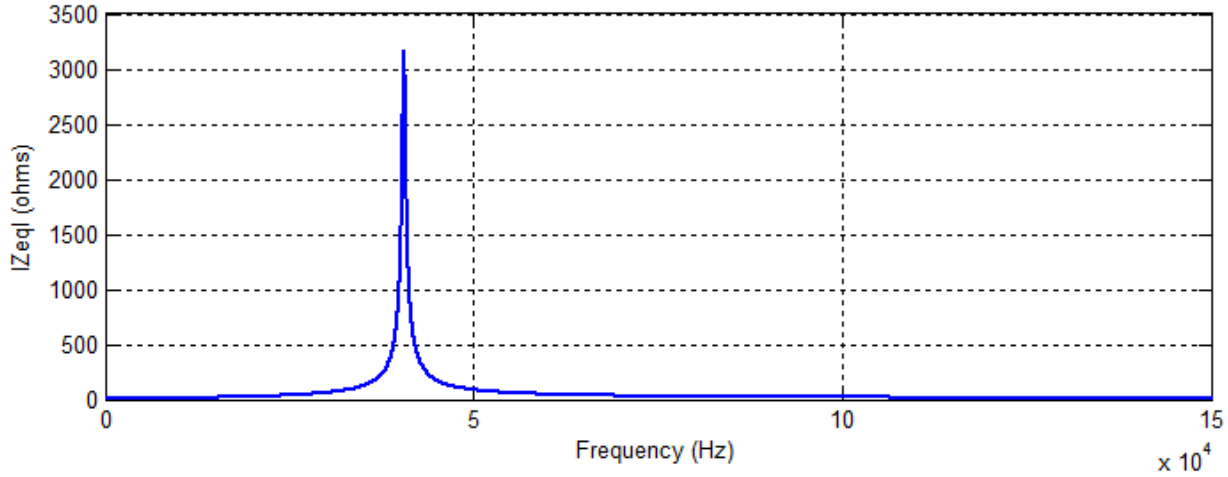

Fig. 2-13 Impedance characteristic in PP topology

It can be observed in the previous figures that, as expected from resonance theory, primary series compensation has minimum equivalent impedance at resonant frequency, leading to a higher value of current at the input of the circuit and also a higher power transfer capability. On the other hand, primary parallel compensation has maximum equivalent impedance at resonant frequency, leading to a low value of current and also a lower power transfer capability. A strong advantage that primary series compensation has over primary parallel compensation is that the compensation capacitance does not depend on the load. This can be seen in table 2-4, where the equations to calculate the value of the capacitor for primary compensation are shown for each topology.

Table 2-4 Equations to calculate Capacitance for primary compensation

Topology	Equation for Primary Compensation
SS	$C_1 = \frac{1}{{\omega_o}^2 L_1}$
PS	$C_1 = \frac{L_1}{\left(\frac{{\omega_o}^2 M^2}{R_{ac}}\right)^2 + {\omega_o}^2 {L_1}^2}$
SP	$C_1 = \frac{1}{{\omega_o}^2 \left(L_1 - \frac{M^2}{L_2}\right)}$
PP	$C_1 = \frac{L_1 - \frac{M^2}{L_2}}{\left(\omega_o L_1 - \frac{\omega_o M^2}{L_2}\right)^2 + \left(\frac{M^2 R_{ac}}{{L_2}^2}\right)^2}$

Additionally, the curve characteristics of the power factor for each topologies are also shown in the following figures.

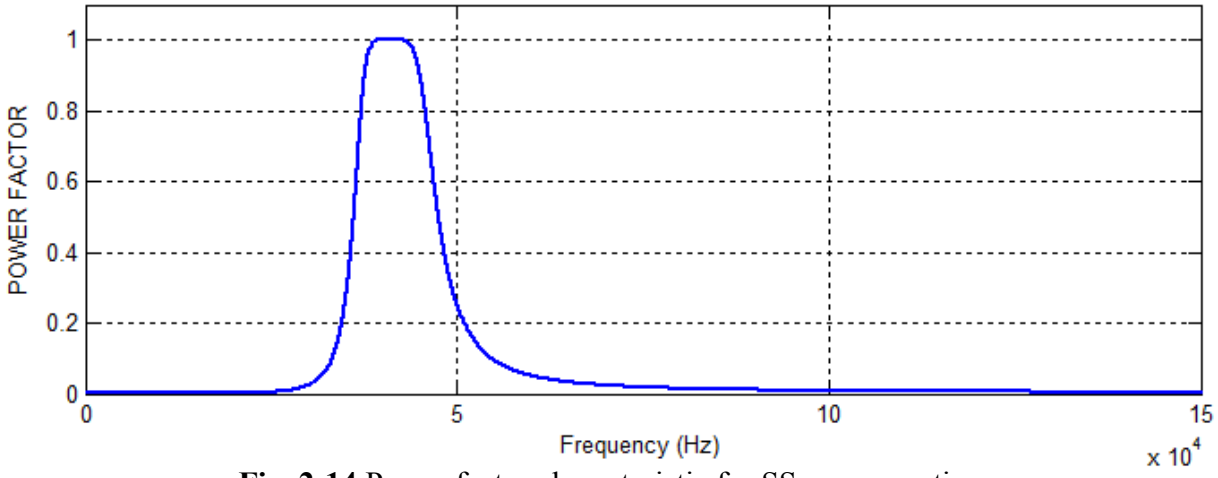

Fig. 2-14 Power factor characteristic for SS compensation

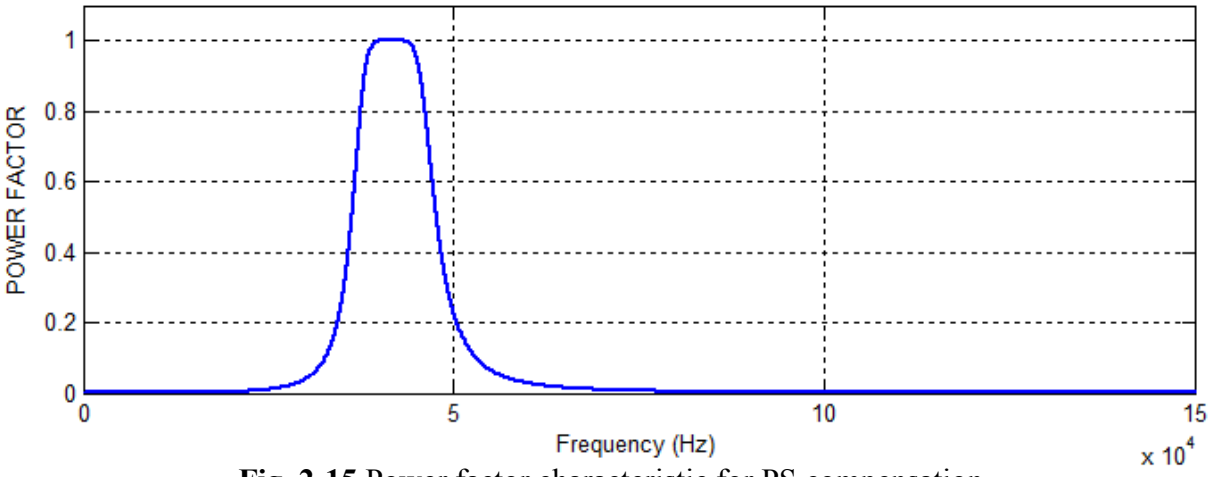

Fig. 2-15 Power factor characteristic for PS compensation

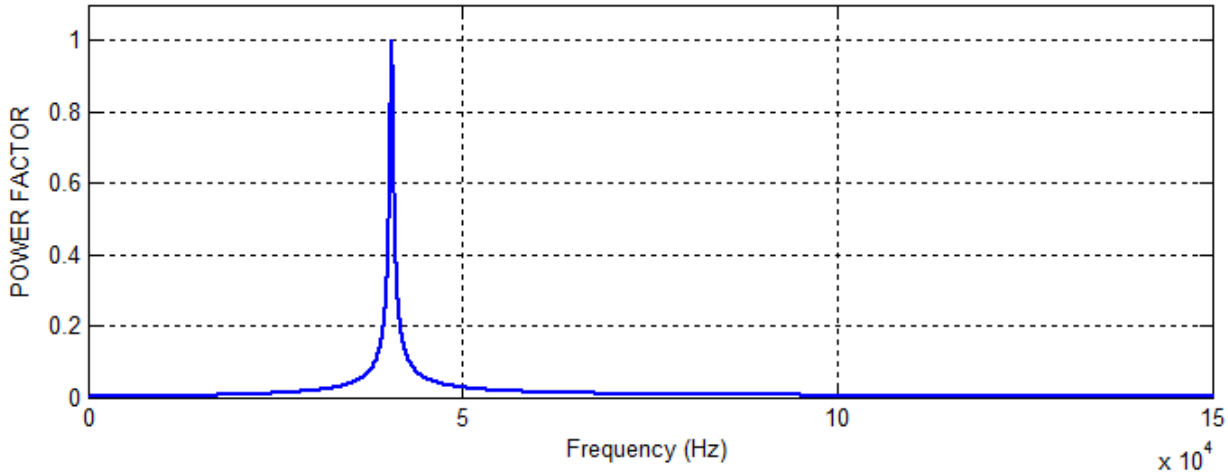

Fig. 2-16 Power factor characteristic for SP compensation

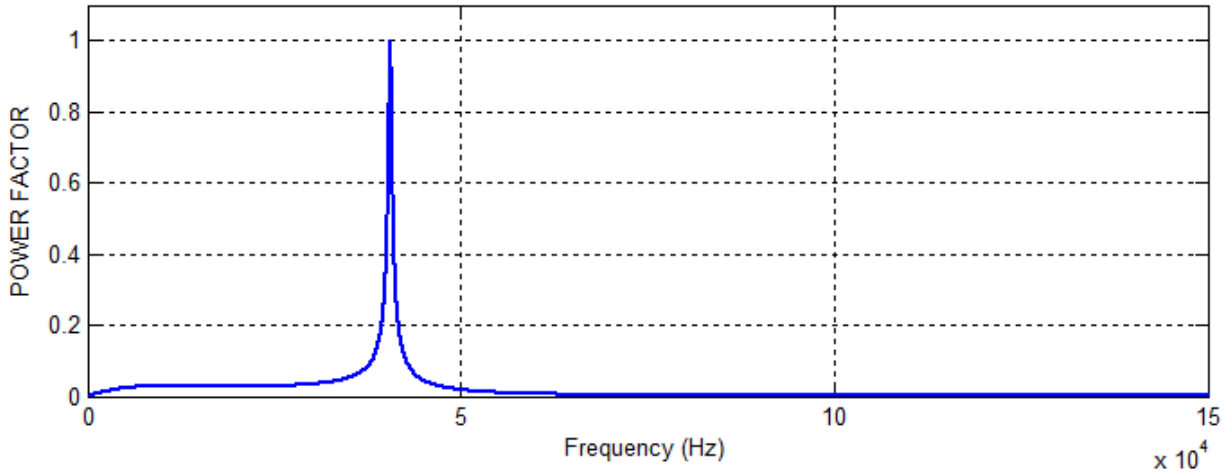

Fig. 2-17 Power factor characteristic for PP compensation

It can be seen from the previous figures, how the power factor becomes unity at the resonant frequency for all topologies. Therefore, the analysis to achieve ZPA in order to increase the power transfer capability of an IPTT is being validated with these figures.

2.5 Selection of Topology

As it has been reviewed, there are four topologies that can be used to improve the power transfer capability in an IPTT: series-series (SS), parallel-series (PS), series-parallel (SP) and parallel-parallel (PP).

Based on the definition of primary and secondary compensation and the equivalent impedance characteristics studied before, the following analysis can be done:

For secondary compensation, it is already known that improves the power transferred to the load. In a secondary series compensation, the voltage induced in the secondary coil will be equal to the open circuit voltage (V_{OC}), having a voltage source characteristics. This is because the reactance of the secondary coil will cancel with the reactance of the capacitor for secondary compensation at resonant frequency. In a secondary parallel compensation, the current in the secondary coil will be equal to the secondary short circuit current (I_{SC}). This is because the

susceptance of the secondary coil will cancel with the susceptance of the capacitor for secondary compensation at resonant frequency, having a current source characteristics [13]-[14].

For primary compensation, it was mentioned before that the objective is to reduce the VA ratings which will be beneficial to the power supply of the IPTT. In a primary series compensation, as it was seen in the impedance characteristics figures, the equivalent impedance is minimum, therefore reducing the voltage rating of the power supply. In a primary parallel compensation, the equivalent impedance is maximum, resulting in a low current rating of the power supply [13]-[14].

Based on these analysis, the topology selected will be series-series (SS). This is because of the following specific reasons:

1. The compensation capacitances, C_1 and C_2 , have no dependency on load variations.
2. The reflected impedance is purely resistive at resonant frequency. This can be validated in equation 8.
3. Higher power transfer capabilities compared to other topologies, which suits perfectly for an initial experimental setup.

The following figure shows the circuit representation of the SS topology. This topology will be analyzed more in detail in the next sections of this thesis.

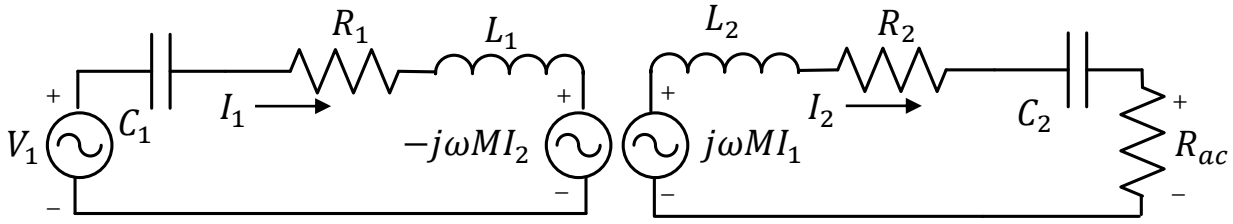

Fig. 2-18 Circuit of IPTT with SS compensation

2.6 Optimal Operation Point Strategy

The optimal operation point in an IPT system with SS compensation can be determined. This condition is defined by the efficiency of the IPTT, which will depend on the operational frequency (f). Additionally, the great advantage of this strategy is that shows the efficiency profile of the IPTT for a range of frequencies. Therefore, it becomes very easy to decide the most ideal resonant frequency for the system.

The first step is to derive the equation for the efficiency based on the compensated topology selected. For the SS topology, the efficiency of the system can be represented as follows:

$$\eta = \frac{{I_2}^2 R_{ac}}{{I_1}^2 R_1 + {I_2}^2 R_2 + {I_2}^2 R_{ac}} \tag{26}$$

From the equivalent circuit shown in figure 2-4, and assuming operation at resonant frequency, the following equation can be derived:

$$\frac{I_1}{I_2} = \frac{R_2 + R_{ac}}{\omega_o M} \tag{27}$$

Arranging equation 26 and substituting equation 27 in equation 26. The resulting equation of efficiency for a SS topology will be:

$$\eta = \frac{R_{ac}}{(R_{ac}+R_2)\left(1+\frac{R_1(R_2+R_{ac})}{{\omega_o}^2 M^2}\right)} \tag{28}$$

It can be seen that the efficiency will be maximum when $\left(\frac{R_1(R_2+R_{ac})}{{\omega_o}^2 M^2}\right)$ tends to zero. Therefore, for maximum efficiency $f_o >> \frac{\sqrt{R_1(R_2+R_{ac})}}{2\pi M}$

Based on this, it can be said that the maximum theoretical efficiency for a SS topology will be:

$$\eta_{max} = \frac{R_{ac}}{R_2 + R_{ac}} \tag{29}$$

For the circuit shown in figure 2.18, using the values from tables 2-2 and 2-3. Its efficiency profile for a range of frequencies from 0 kHz to 150 kHz will be as follows.

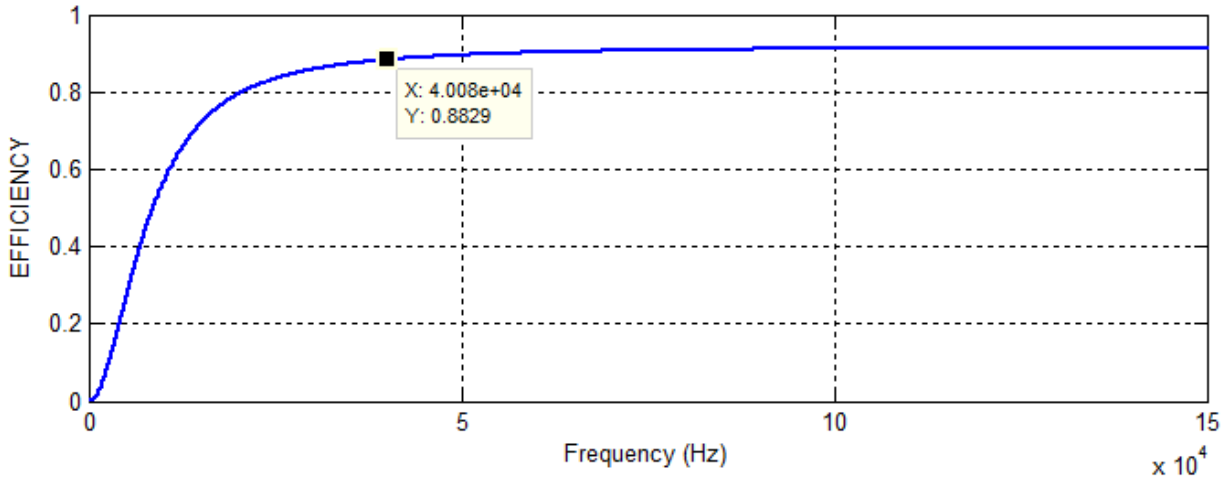

Fig. 2-19 Efficiency profile of IPT system example

Figure 2-19 shows how for a range of frequencies, the efficiency will behave for this example. As mentioned before, the load has been fixed at 1.3 Ω. From the figure, it can be seen that at a frequency of 40 kHz, the efficiency will be around 88.3%. This value can also be calculated from equation 28. Additionally, using equation 29, the maximum theoretical efficiency is 91.71%, but this condition is achieved at a frequency around 1 GHz.

A 3D plot can also be obtained by also varying the load. This could give an overview of how the efficiency behaves for different loads and frequencies. Figure 2-20 shows the results for the same values as before. But also varying the load from 0 to 20 Ω.

It has been proved that it is possible to determine an optimal operation point for a SS compensated IPT system. This strategy shows the efficiency profile of the system at different frequencies, giving a good overview of which conditions should be established in order to increase the performance of the system.

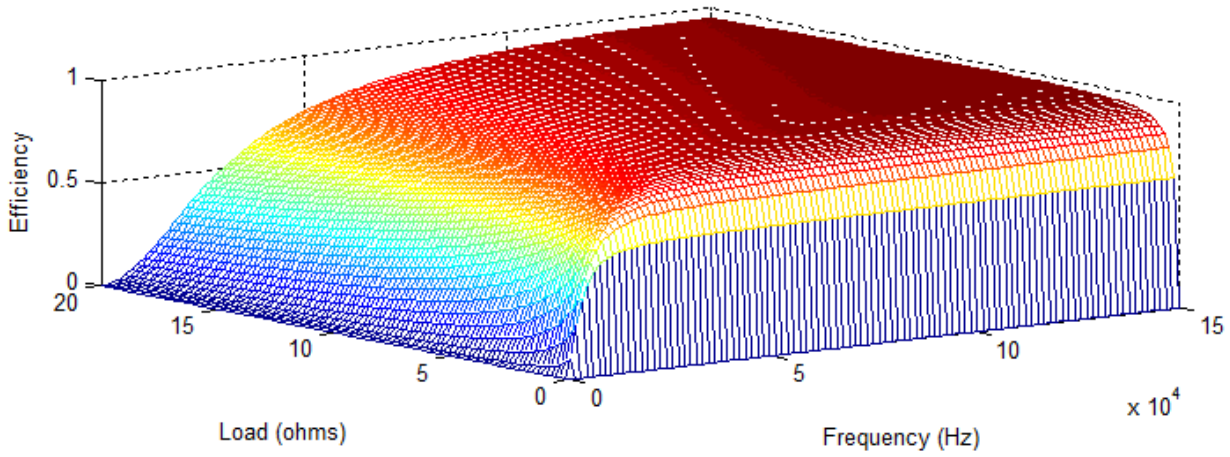

Fig. 2-20 3D efficiency profile of IPT system example

2.6.1 TUNING AND RESONANT CONSIDERATIONS

An optimal operation point has been determined based on the efficiency of the system. However, it also important to determine the ideal point of operation based on the primary and secondary loaded quality factors (Q_1, Q_2). This analysis is very important for systems that operate at a fixed frequency control, because it is convenient to ensure a stable point of operation.

From resonant circuit theory, if a loaded quality factor is too high, the resonant bandwidth will be reduced. Therefore, a minor frequency deviation from the resonant frequency can cause the power transfer capability to drop drastically. Additionally, in practice, systems with higher loaded quality factor values may be too critical to tune [13]-[15].

On the other hand, it is known from the theory of series resonant inverters, that the loaded quality factor should be high enough for the current in the resonant circuit to be sinusoidal (for example Q_1>= 2.5) [13]-[15]. These analysis can be validated in the following figures.

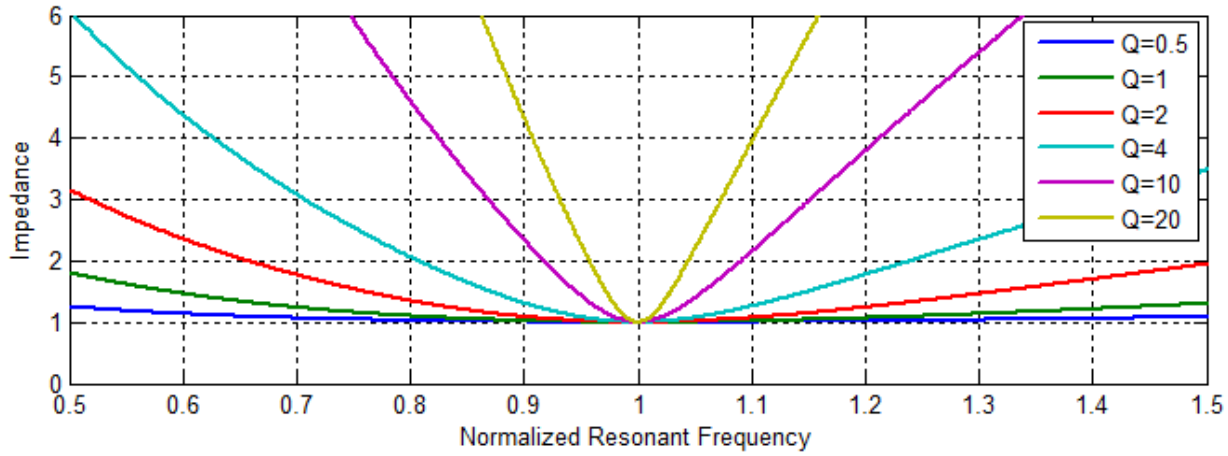

Fig. 2-21 Effect of Q in a series resonant circuit

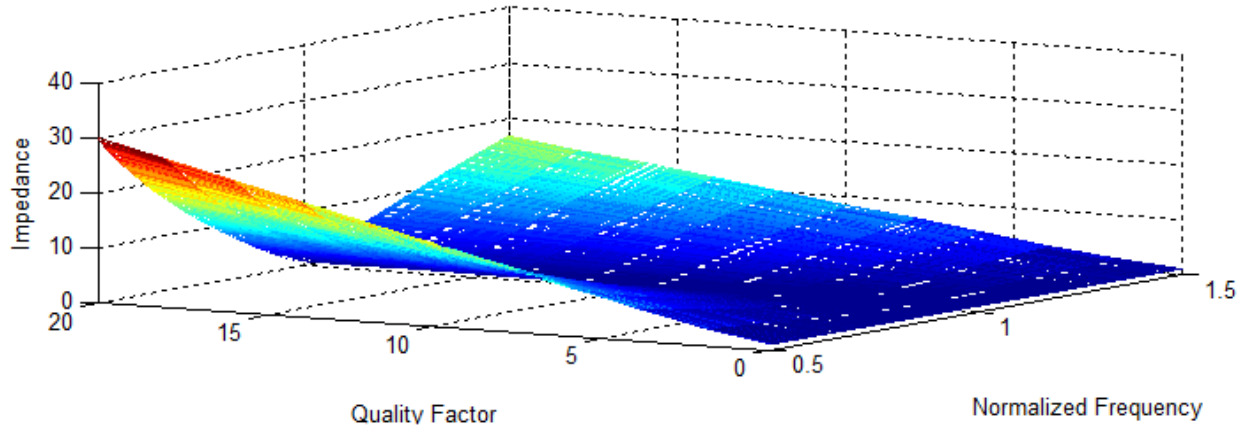

Fig. 2-22 Effect of Q in a series resonant circuit (3D)

These figures were plotted from the following derivation:

Considering a LCR resonant circuit:

$$Z = \frac{1}{j\omega C} + j\omega L + R \tag{30}$$

Equation 30 can also be expressed as:

$$Z = R + j\left(\omega L - \frac{1}{\omega C}\right) = R\left[1 + jQ\left(\frac{\omega}{\omega_o} - \frac{\omega_o}{\omega}\right)\right] \tag{31}$$

2.7 Design of a Series-series Compensated IPTT

In this section, the theory that has been studied will be validated throughout analytical calculations and software simulations. The simulations will be made in Simulink.

The starting point will be to obtain the parameters of an IPTT. Therefore, two circular coils were built in the laboratory and their parameters were measured resulting in the values shown in table 2-2. The details of the coils construction will be reviewed in chapter 4.

Now that the IPTT parameters are known, the next step will be to define the optimal operation point, based on the efficiency of the system. This will depend on the operational frequency and load.

As was mentioned before, the load was fixed at 1.3 Ω. In practice, three power resistors were used to give an overall load characteristic of 30 W. The efficiency profile for these values was shown in figure 2-19. Where the efficiency was around 88.3% at 40 kHz.

Based on this, the initial values of the compensation capacitors can be calculated using equations 9 and 13. Giving the results shown in table 2-3.

Now, the tuning and resonant considerations need to be verified. As mentioned before, in a series-series compensation topology, if the secondary compensation is tuned, then the primary equivalent side can be represented as follows.

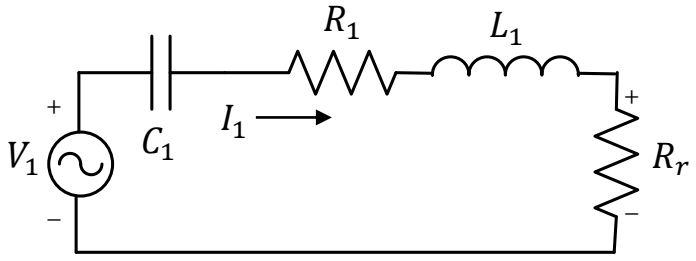

Fig. 2-23 Primary equivalent circuit when secondary compensation is tuned

It can be seen that R_r is the reflected impedance in the primary side. The primary and secondary loaded quality factor can be calculated as follows [3]-[9]-[12]:

$$Q_1 = \frac{\omega L_1}{(R_1 + R_r)} \quad (32) \qquad \text{where,} \qquad R_r = \frac{\omega^2 M^2}{(R_2 + R_{ac})} \quad (33)$$

$$Q_2 = \frac{\omega L_2}{(R_2 + R_{ac})} \quad (34)$$

Using these equations, the results are: $Q_1 = 4.7073$ and $Q_2 = 4.1241$. Based on these results, the tuning and resonant considerations are satisfied. Therefore, a stable point of operation is ensured and the primary current will have a sinusoidal waveform.

In a secondary series compensation system, the Thevenin's theorem can be used to simplify the analysis [14]. Figure 2-21 shows the Thevenin's equivalent circuit for secondary series compensation. Like it was mentioned before, the reactance of the secondary winding will cancel with the reactance of the capacitor at the resonant frequency. Also, the induced secondary voltage is equal to $V_2' = \omega_o M I_1$. Assuming that V_2' is sinusoidal, the following equation can be derived.

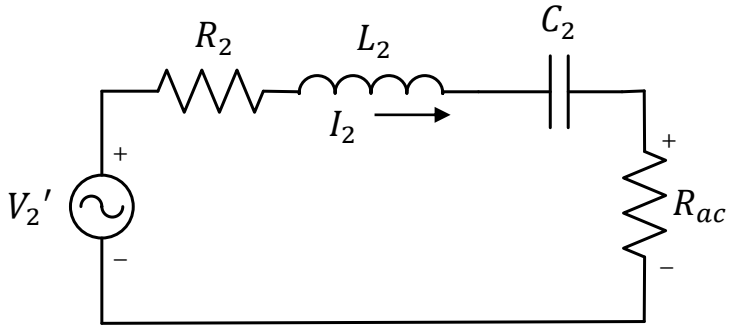

Fig. 2-24 Thevenin's equivalent circuit in secondary series compensation

$$I_2 = \frac{V_2'}{R_2 + R_{ac}} = \frac{\omega_o M I_1}{R_2 + R_{ac}} \quad (35)$$

Now, based on basic circuit analysis and the equations shown before, the theoretical values of the SS compensated IPTT can be calculated. For this analysis, a signal generator was used as the source.

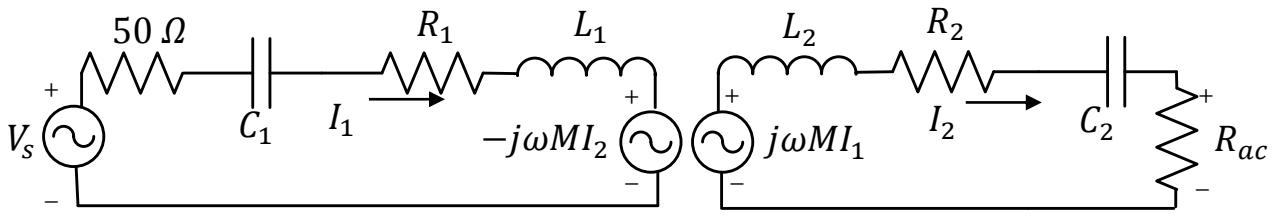

$I_1 = 0.1220$ A $\quad I_2 = 0.2836$ A

$V_s = 7.07$ V $\quad R_{ac} = 1.3\ \Omega$

$f = 40\ kHz \quad \eta = 88.28\ \%$

Fig. 2-25 Theoretical values of the IPT system

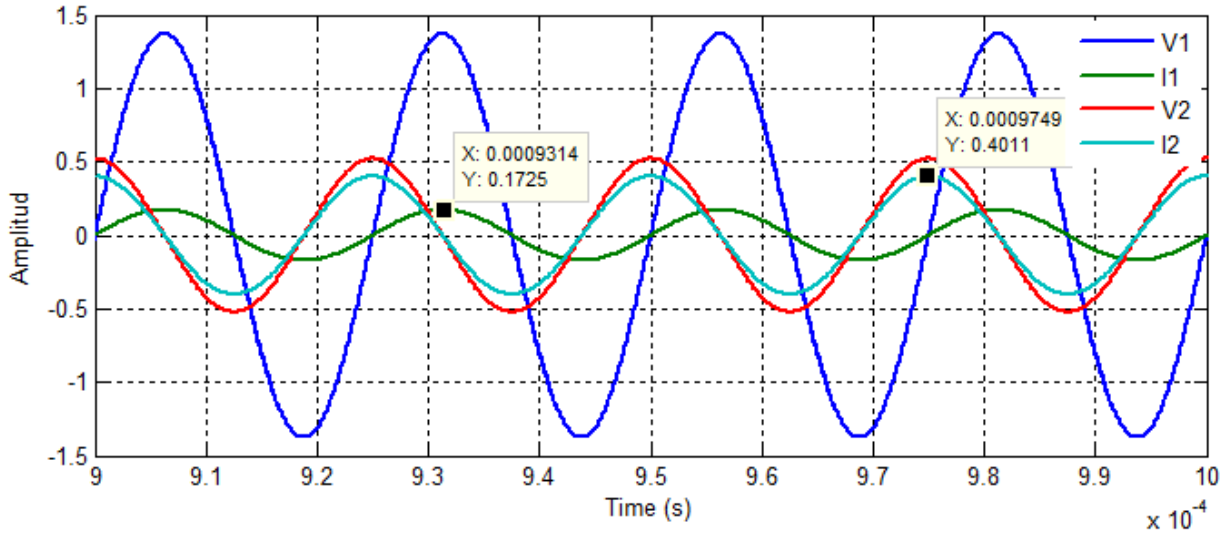

Fig. 2-26 Simulation results of the SS compensated IPT system

It can be seen that the analytical calculations match with the simulation results. This confirms that the equations that were derived are correct and can be used for an optimal design of a SS compensated IPTT.

2.8 Summary

In this chapter, the fundamentals of inductive power transfer technology were reviewed, covering the following points: the coupling model, the derivation of the equivalent circuit, capacitive compensation, the different topologies that can be used and the effect of the equivalent impedance in the circuit. Subsequently, the SS compensation topology was chosen for the design, based on advantages that were identified for the modeling. Additionally, an optimal operation point strategy was presented and tuning and resonant considerations were proposed. Finally, all the concepts, design considerations and techniques were validated with simulation results made in the software Simulink, for the SS compensated IPTT, giving an efficiency of 88.28%.

CHAPTER 3

POWER SUPPLY OF AN IPT SYSTEM

3.1 Introduction

The power supply of IPT systems consists of a stable DC voltage source connected to an inverter, to produce an AC signal at frequencies of kHz range. For this study, a full bridge inverter is selected, because it offers more control possibilities and its output voltage is doubled compared to the half bridge inverter [16]. The last point will increase the power ratings of the system.

A series-series IPT system, when connected to a full bridge inverter, can be seen and analyzed as a class D voltage switching series resonant inverter [15]. This is because of the resonant characteristics of the IPT system studied in chapter 2. Therefore, the semiconductors will be switching at resonant frequency.

The following figure shows a full bridge inverter connected to a SS compensated IPTT. The inverter is operating at resonant frequency, therefore each pair of switches is ON for one half cycle (180°). Resulting in a square wave output voltage [16].

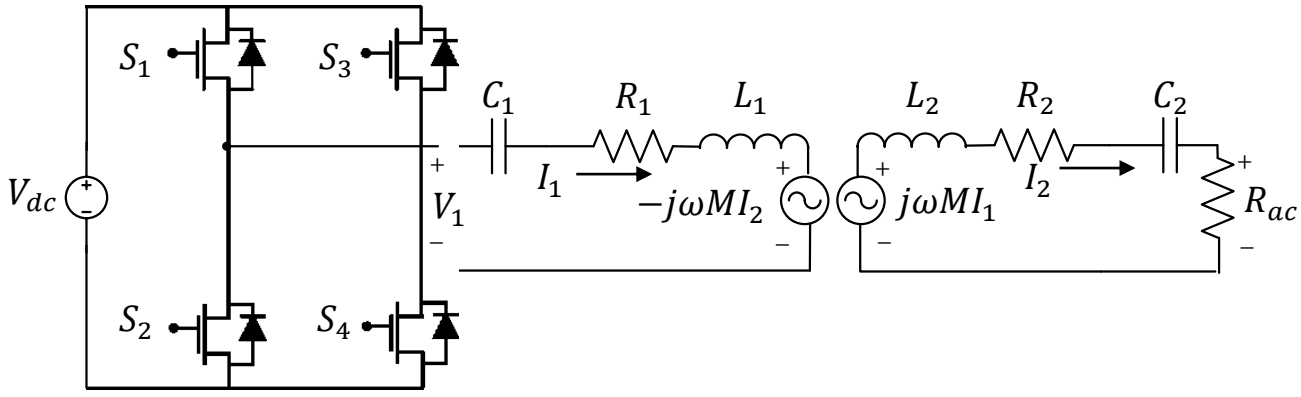

Fig. 3-1 Full bridge inverter connected to a SS compensated IPTT

As a general characteristic of this class of inverter. Like it was mentioned and analyzed in chapter 2, if the loaded quality factor is high enough, the current that feeds the IPTT will be sinusoidal and the current through the semiconductors will be half wave sinusoidal. Additionally, the voltages through the switches will be square wave [15].

A main advantage of this class of inverters, is that the voltage across the semiconductors is equal to the supply voltage, which is suitable for high voltage applications. Additionally, low voltage MOSFET's can be used, because they have fast switching speeds and their on-resistances is low, which reduces the conduction losses and junction temperatures, resulting in higher efficiencies [15].

In this type of inverter, the output voltage can be regulated by different types of control techniques, where each has their own advantages and disadvantages. In this study, the type of control that was selected is called optimum asymmetrical voltage cancellation (o_AVC) control. This control technique is a particular case of one of various types of fixed frequency control that can be used in full bridge resonant inverters. More details about this type of control technique will be explained in this chapter.

3.2 Analysis of Operation

It is known from fourier series analysis, the output voltage of the full bridge inverter will be [16]:

$$V_1(t) = \frac{4V_{dc}}{\pi} \sum_{n=1,3,5\ldots} \frac{1}{n} \sin(n\omega_s t) \tag{36}$$

It can be seen from equation (36) that the voltage spectrum contains the fundamental and only odd harmonic components. However, since the primary has low harmonic distortion and is

sinusoidal, because of the conditions mentioned in chapter 2, it can be said that no losses are generated other than the fundamental component. Additionally, because of the filtering effect of the IPTT (resonant circuit), the secondary current will have even a lower harmonic distortion.

Moreover, it is also well known from fourier series analysis, that the fundamental component of the output voltage of the full bridge resonant resonant inverter can be defined as [16]:

$$V_{1(1)} = \frac{4}{\pi\sqrt{2}} V_{dc} \tag{37}$$

Based on this, the series-series IPTT that was reviewed in chapter 2, can now be analyzed connected to a power supply at resonant frequency. But now, the load will be driven to its rating power (30 W). Using the equations derived in chapter 2 and equation 37, the theoretical values were calculated, giving the results shown in the following figure.

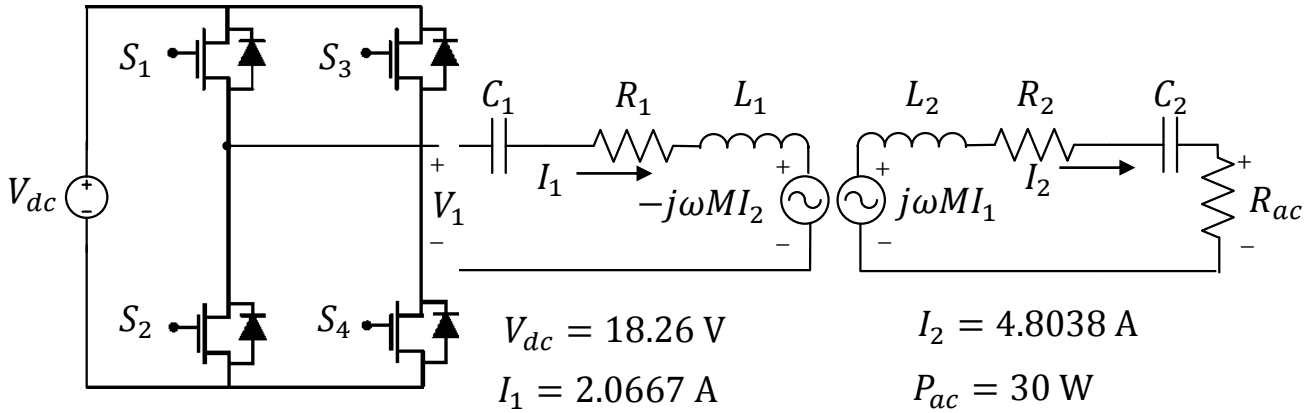

Fig. 3-2 Theoretical values of the IPT system fed by a power supply

It can be seen in figure 3-2, that the minimum DC voltage needs to be $V_{DC} = 18.26$ V, in order to supply rated power. Additionally, the efficiency of the system is $\eta = 88.28$ % as it was

calculated before. It is important to remember that both coils are separated by a 25 mm air gap, and that the inverter will be switching at resonant frequency ($f_s = f_o$), therefore it is expected to see a square wave voltage at the output of the inverter in phase with the primary current. With these values of current in the primary and secondary side, the expected efficiency is obtained. The simulation results of the circuit are shown in the following figure.

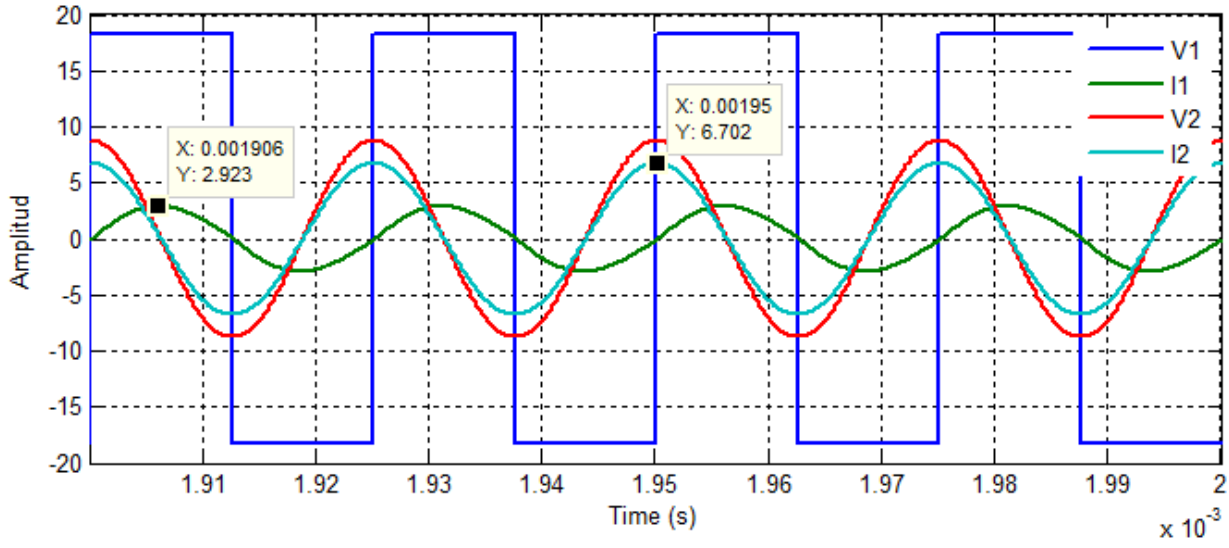

Fig. 3-3 Theoretical values of the SS compensated IPTT fed by a power supply

It can be seen in figure 3-3, that the primary current is sinusoidal. Also, the theoretical values match with the simulation results, validating the analytical calculations. From these simulation results, the load is being driven to its rated power of 30 W, and the IPTT is operating at an efficiency of $\eta = 88.28\ \%$. Additionally, to validate equation 37 an FFT analysis for the primary current (I_1) and primary voltage (V_1) was performed in Simulink. Showing the following results.

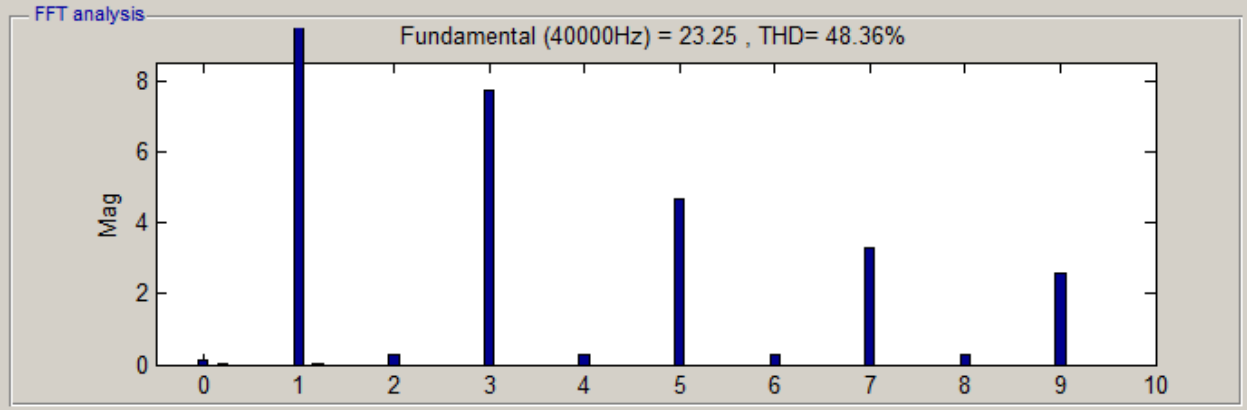

Fig. 3-4 FFT analysis results of primary voltage (V_1)

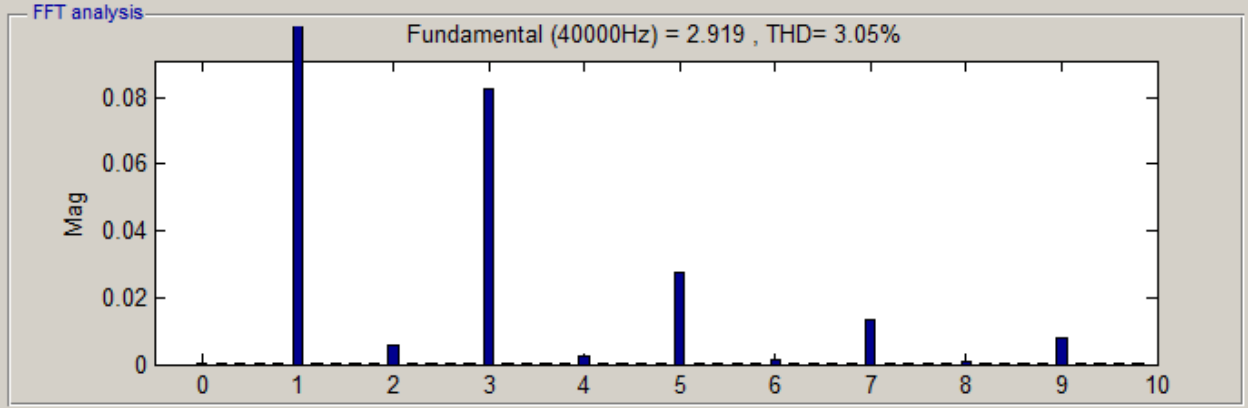

Fig. 3-5 FFT analysis results of primary current (I_1)

Figure 3-4, confirms that the primary voltage contains only odd harmonic components. Additionally, it can be seen that the magnitude of the fundamental component matches with the result from equation 37 ($V_{1(1)}$ = 16.44 V).

In the same way, figure 3-5, confirms the magnitude of the primary current, I_1 = 2.06 A, and also shows that the THD = 3.05 %. Which ratifies a low harmonic distortion, as expected from the analysis made before.

The following figure, shows the waveforms in one leg of the inverter and the output waveforms of the inverter obtained in the simulation. This figure validates the theory of operation in a series resonant inverter operating at resonant frequency ($f_s = f_o$).

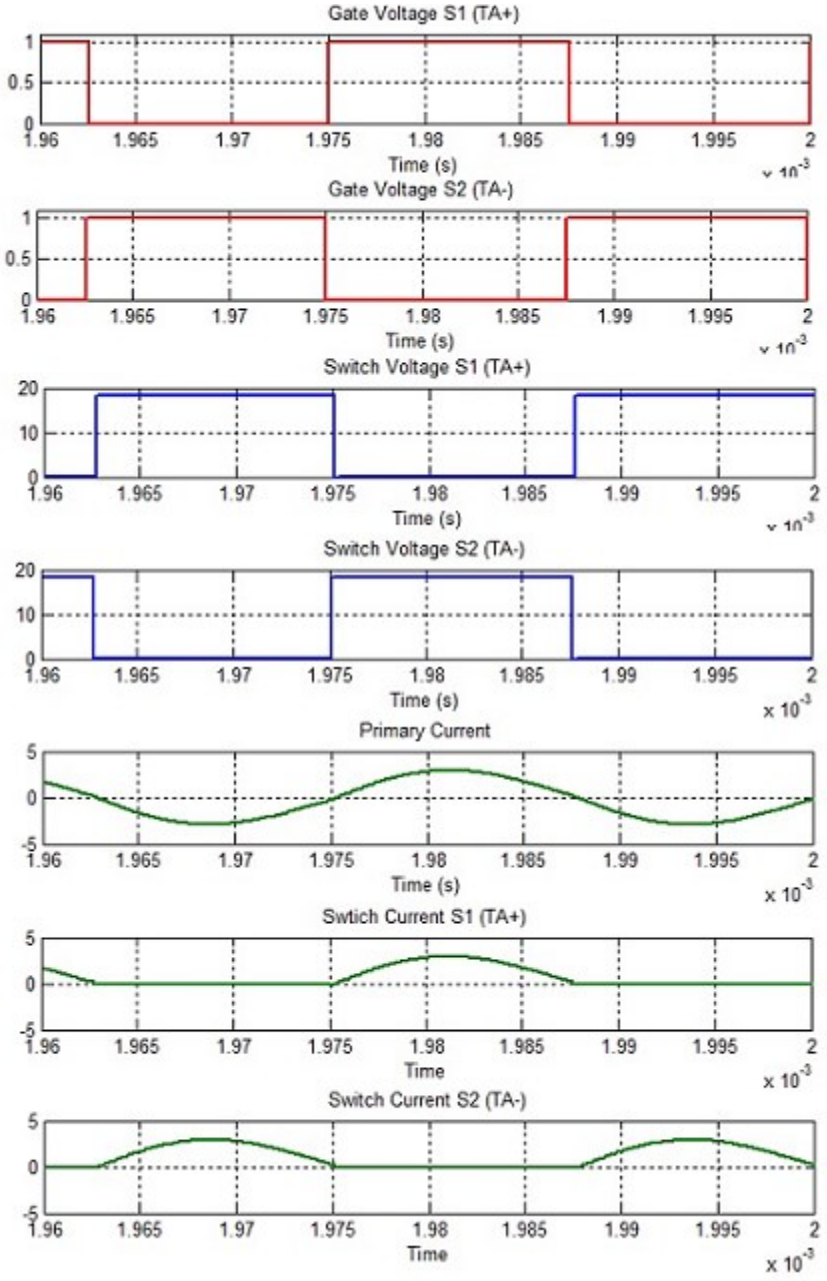

Fig. 3-6 Waveforms in one leg and output of inverter obtained in simulation ($f_s = f_o$)

3.3 Voltage Regulation

As it was mentioned before, the output voltage of the inverter can be regulated in order to control the power flow of the system and operate at desired values. They are three ways to achieve

this: by varying the DC link voltage, controlling the switching frequency or controlling the phase shift between the two legs of the inverter (fixed frequency control).

Varying the DC link voltage will require an additional power electronic device, for example a DC-DC converter. Therefore, this option will not be considered in this study. The most common control strategies in this type of applications are: variable frequency control and fixed frequency control.

Initially, the IPT system that is being studied will not have dynamic variations in its parameters, like mutual inductance (M) or load (R_{ac}). Therefore, there is no need to implement a variable frequency control. The most simple and effective way to do voltage regulation is by implementing a fixed frequency control strategy. Additionally, with fixed frequency control, no attention needs to be taken on the phenomenon of bifurcation [17].

However, special attention needs to be made in the switching losses of the semiconductors while regulating. An undesired characteristics on fixed frequency control is that hard switching will be present. Therefore, the implementation of soft switching techniques is essential [18].

Because of the characteristics of the resonant inverter with the IPTT, zero voltage switching (ZVS) operation seems to be a good option to minimize the switching losses. This means that the switching frequency (f_s) needs to be higher than the resonant frequency (f_o). Even though the power transfer capability will be lightly decreased, the main objective is to maintain a high overall performance of the system.

It is known that in a fixed frequency control, the semiconductors in the two legs of the inverter are controlled separately. This will allow the output voltages in each leg to overlap with each other by an angle α. During this overlap interval, the output voltage of the inverter will be zero, generating a quasi-square waveform. This is because the both top semiconductors or the both

bottom semiconductors will be ON at the same time [16]. When α = 0°, no overlapping will occur, and the output voltage waveforms will be square, as it was observed in figure 3-3. This is called conventional phase shift control or voltage cancellation control.

Throughout time, other two methods have been developed in order to improve the performance of operation in a fixed frequency control for series resonant inverters. Each method or strategy operates by the same principal as the conventional strategy, but controlling different variables. In summary, three control strategies can be considered: the conventional phase shift control (PS) [21]-[22]-[23], asymmetrical duty cycle control (ADC) [24]-[28]-[29] and asymmetrical voltage cancellation control (AVC) [25]-[30]-[31]. By using one of these control strategies, the output voltage waveforms of the inverter, will be determined by the following control angles:$\alpha_+, \alpha_-, \beta$. Figure 3-7 shows a quasi-square waveforms with the representation of the three control angles [19].

The characteristics of the control angles in each control strategy are presented as follows:

1. Phase shift control (PS): α = α_+ = α_- vary between 0° and 180°. Also, β = 180° constant.
2. Asymmetrical duty cycle control (ADC): α_+= α_- = 0° constant. β varies between 0° and 180° and finally, α = 180°- β.
3. Asymmetrical voltage cancellation control (AVC): β varies between 0° and 180°, $\alpha_+ \leq \beta$ and $\alpha_- \leq 360° - \beta$.

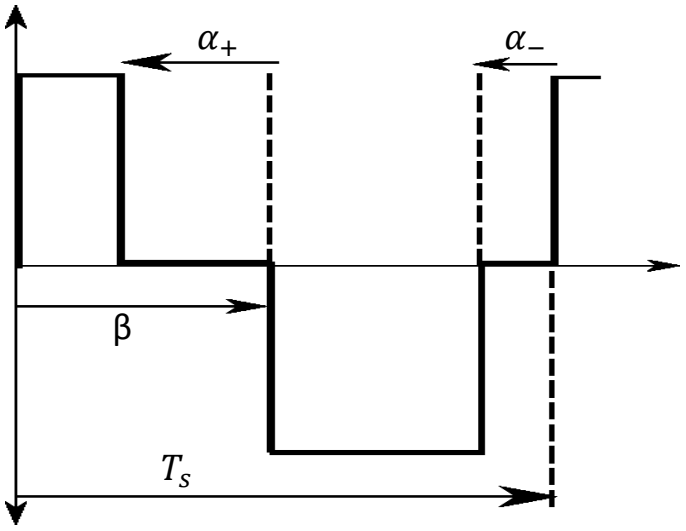

Fig. 3-7 Quasi-square waveform with the control angles

The typical waveforms for each control strategy, as well as the gate signals in each semiconductor, are shown in figure 3-8.

3.3.1 OPTIMUM ZVS CONTROL STRATEGY

As it was mentioned before, there are three fixed frequency control strategies that can be used to regulate the output voltage of the inverter, and therefore the power flow of the system: PS control, ADC control and AVC control. Additionally, ZVS operation in all active semiconductors is required to minimize the switching losses. Therefore, an analysis is made in order to determine an optimum ZVS control strategy that suits the IPT system requirements [18]-[19]-[20].

In steady state, the output voltage of the inverter can be represented by the following fourier series [19]:

$$\widehat{V_{1h}} = \frac{V_{dc}}{h\pi}\sqrt{{a^2}_h + {b^2}_h} \tag{38}$$

$$\phi_{vh} = tan^{-1}\left(\frac{a_h}{bh}\right) \tag{39}$$

Where, the amplitude and phase of the h_{th} harmonic of V_1 are denoted as V_{1h} and ϕ_{vh} respectively. Also:

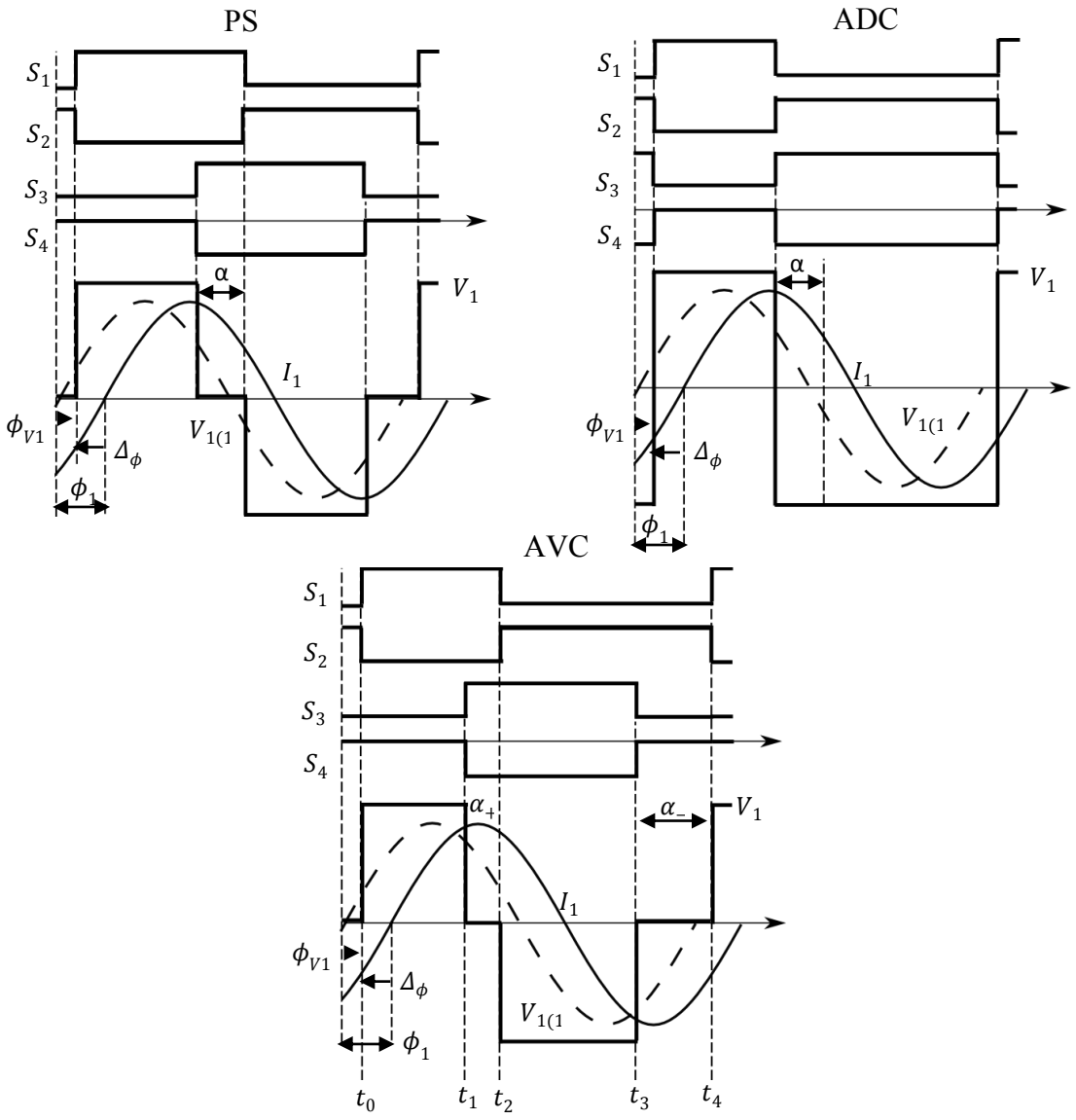

Fig. 3-8 Typical waveforms of the three fixed frequency control strategies

$$a_h = \sin(h(\beta - \alpha_+)) + \sin(h\beta) + \sin(h\alpha_-) \tag{40}$$

$$b_h = 1 - \cos\big(h(\beta - \alpha_+)\big) - \cos(h\beta) + \cos(h\alpha_-) \tag{41}$$

Additionally, the output current can be expressed as:

$$i_1(t) = \widehat{I_1} sin(\omega_s t - \Delta\phi) \tag{42}$$

Where $\widehat{I_1}$ is the amplitude of the output current that, as it was reviewed before, it is assumed to be sinusoidal, ω_s is the switching frequency, and the phase will be:

$$\Delta\phi = \phi_1 - \phi_{v1} \tag{43}$$

$$\phi_1 = tan^{-1}\left(Q_1\left(\omega_n - \frac{1}{\omega_n}\right)\right) \tag{44}$$

The phase lag ϕ_1 between $V_{1(1)}$ and I_1 can be obtained from equation 44. It is important to mention that ω_n is the normalized switching frequency. Figure 3-9 gives a graphical representation of $\Delta\phi$, $\phi_1$and ϕ_{v1}.

From [18]-[19], the condition to achieve ZVS operation in all semiconductors is:

$$\Delta\phi = \phi_1 - \phi_{v1} > 0 \tag{45}$$

In order to satisfy equation (45), one approach could be to increase ϕ_1, by also increasing the switching frequency (equation 44). However, this will result in higher conduction and turn-off losses, since the current needs to be higher to transfer the same amount of power. Therefore, it can be said that the inverter should operate at the minimum switching frequency possible above the resonant frequency and with $\phi_1 > \phi_{v1}$, to maintain ZVS operation [18]-[19].

Based on this, a better approach will be to decrease ϕ_{v1}, which depends on the control angles $\alpha_+, \alpha_-, \beta$. This can be validated by substituting equations 40 and 41 in equation 39 for the fundamental component.

$$\phi_{v1} = tan^{-1}\frac{sin(\beta-\alpha_+)+sin\beta+sin\alpha_-}{1-cos(\beta-\alpha_+)-cos\beta+cos\alpha_-} \tag{46}$$

From equation 46, it can be said that an optimum control strategy to maintain ZVS will be the one that minimizes ϕ_{v1} by varying the control angles $\alpha_+, \alpha_-, \beta$. From [19], it can be concluded that the optimum control strategy will be maintaining β=180° constant, and **only** varying the

control angles α_+ or α_- **individually**. This means, looking at figure 3-9, trajectory **AB** and further **BD** if necessary, or trajectory **AC** and further **CD** if necessary. Any other trajectory will maximize ϕ_{v1}. It can be said that this optimum control strategy is a particular case of AVC control. Therefore, it will be called optimum AVC control (o_AVC).

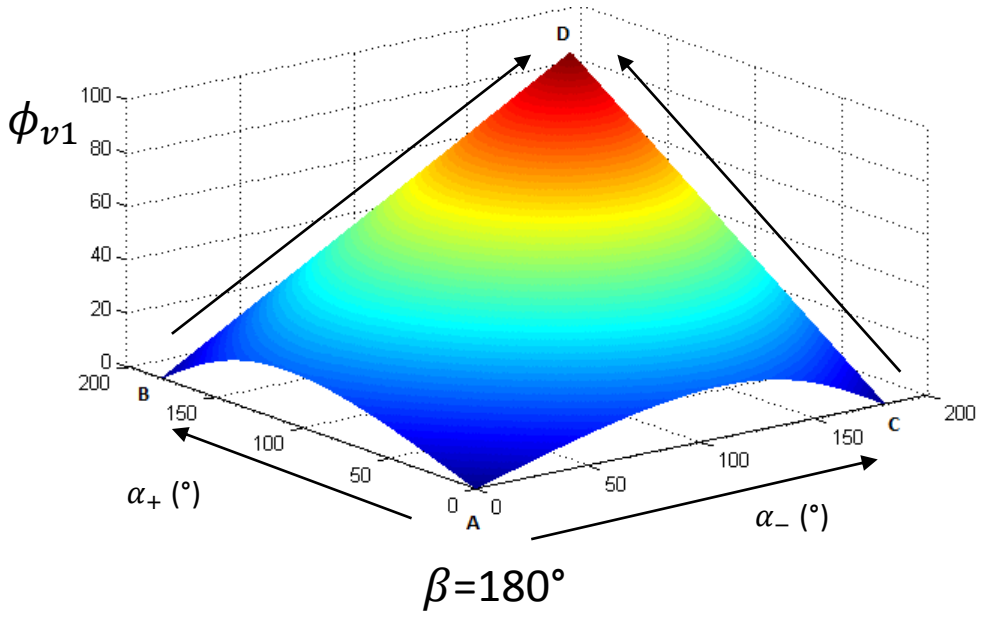

Fig. 3-9 Trajectory of control angles for an optimum control strategy

After this analysis, it can be concluded that there are three control strategies that can be finally considered: PS, ADC and o_AVC control. Figure 3-10 shows the typical waveforms for the o_AVC control strategy.

In order to verify the advantages that o_AVC control has over PS and ADC control, the following analysis will be performed: identify analytically, which strategy minimizes the losses in the semiconductors of the inverter, and therefore improve the performance of the system.

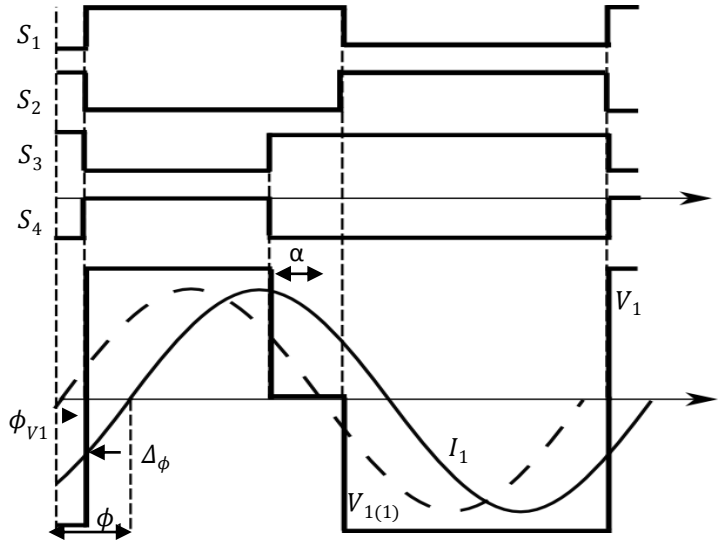

Fig. 3-10 Typical waveforms for the o_AVC control strategy

Each method will be compared based on the condition stated in equation 45, which guarantees ZVS operation.

The first analysis will be made to the behavior of ϕ_{v1} for each control strategy, by using equation 46 and the characteristics of each method mentioned in page 40. The result are plotted in figure 3-11.

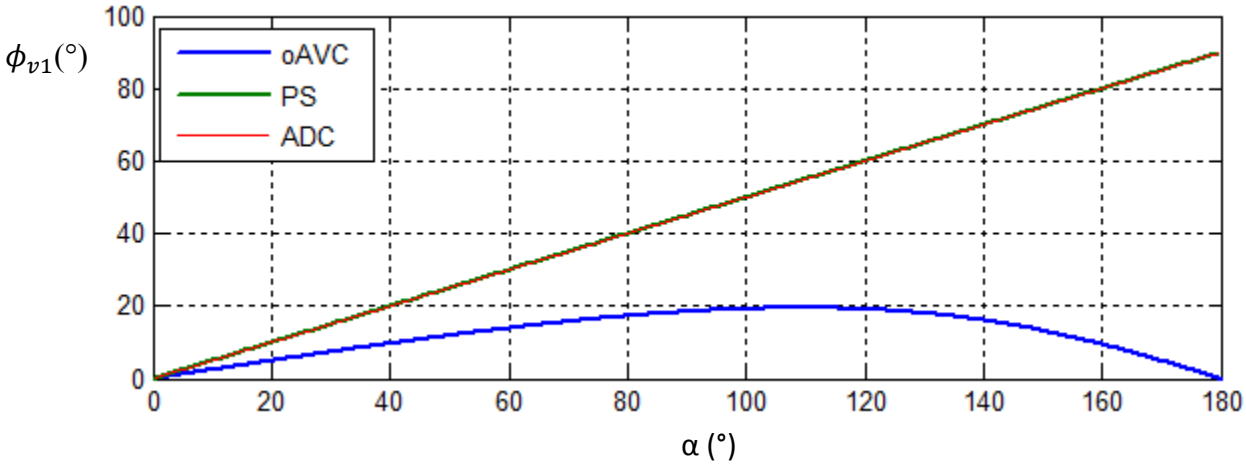

Fig. 3-11 Behavior of ϕ_{v1} in each control strategy

It can be seen in figure 3-11, how ϕ_{v1} increases linearly as α also increases for PS and ADC control. While, on the other hand the maximum value for ϕ_{v1} will be around 20° with α ≈ 110° for o_AVC control. This shows how o_AVC control is more effective in minimizing the value of ϕ_{v1} while varying the control angles $\alpha_+, \alpha_-, \beta$.

Continuing with the analysis; as explained in [18]-[19], the amplitude and phase of the output voltage of the inverter V_{11}, for each control strategy can be obtained by particularizing equations 38 and 39 for each case. This will result in the following equations:

For PS and ADC control:

$$\widehat{V_{11}} = \frac{4V_{dc}}{\pi} cos\frac{\alpha}{2} \tag{47}$$

$$\phi_{v1} = \frac{\alpha}{2} \tag{48}$$

Additionally, the following derivations for PS and ADC control can be done. Substituting equations 44 and 48 in equation 45, will result as:

$$\Delta\phi = tan^{-1}\frac{(\omega_n{}^2-1)Q_1}{\omega_n} - \frac{\alpha}{2} \tag{49}$$

Solving equation 49 for the critical point $\Delta\phi$ =0°, will result in:

$$\omega_n = \frac{tan\left(\frac{\alpha}{2}\right)+\sqrt{tan\left(\frac{\alpha}{2}\right)^2+4Q_1{}^2}}{2Q_1} \tag{50}$$

In the same way, for o_AVC control:

$$\widehat{V_{11}} = \frac{V_{dc}}{\pi}\sqrt{10+6cos\alpha} \tag{51}$$

$$\phi_{v1} = tan^{-1}\frac{sin\alpha}{3+cos\alpha} \tag{52}$$

Substituting equations 44 and 52 in equation 45, will result as:

$$\Delta\phi = tan^{-1}\frac{(\omega_n{}^2-1)Q_1}{\omega_n} - tan^{-1}\frac{sin\alpha}{3+cos\alpha} \tag{53}$$

Solving equation 53 for the critical point $\Delta\phi$ =0°, will result in:

$$\omega_n = \frac{(3-cos\,\alpha)sin\alpha+\sqrt{(cos^2\alpha-6cos\alpha+9)sin^2\alpha+(256+64sin^2\alpha+4sin^4\alpha)Q_1{}^2}}{(16+2sin^2\alpha)Q_1} \tag{54}$$

From equations 50 and 54, it is possible to know the minimum normalized switching frequency (ω_n) required to obtain ZVS operation in the semiconductors of the inverter. As can be seen, these equations depend on α and Q_1. The following figure shows a general plot for these equations for different values of Q_1.

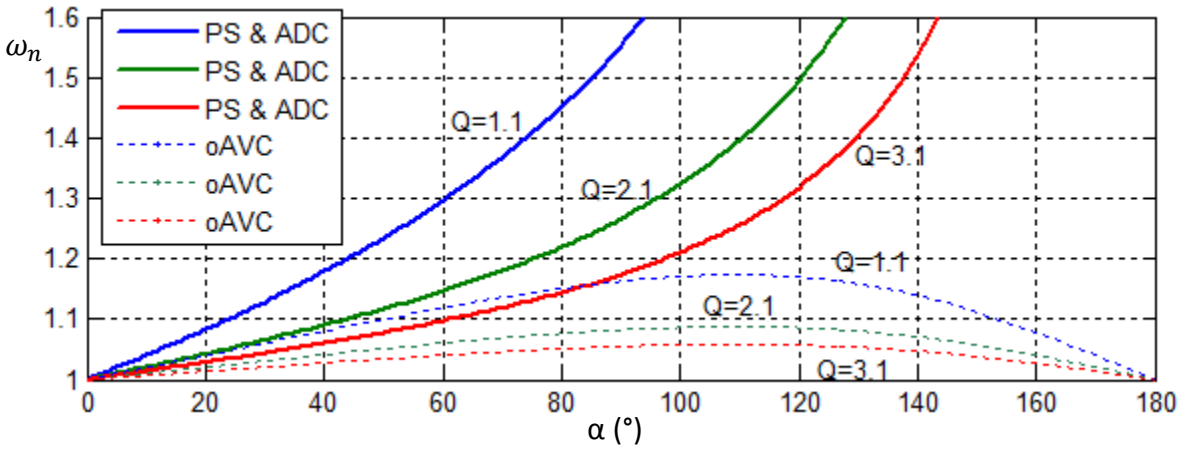

Fig. 3-12 Minimum normalized switching frequency (ω_n) for ZVS

From figure 3-12, o_AVC is the only control strategy that can maintain a minimum normalized switching frequency achieving ZVS operation. For PS and ADC control, the minimum normalized switching frequency increases considerably for higher values of α. This concludes that

by analytical demonstrations, the best effective option is to implement o_AVC control strategy in order to minimize the switching losses in the inverter while regulation the output voltage. An important point about this study is that was performed based on the characteristics of the SS compensated IPTT that is being studied.

3.4 ZVS Verification Technique

In this section, a steady state time domain analysis is performed as in [26]-[27], in order to calculate the switching currents in each semiconductor to verify ZVS operation. This means that the primary current (I_1) can be determined when each active device switches.

It is know that ZVS operation is achieved by turning ON the semiconductor while its antiparallel diode is conducting [15]-[19]. Therefore, four intervals can be defined, which represents the condition for each semiconductor to achieve ZVS.

$$\begin{aligned} i_1(t_0) &< 0 \text{ for S1 (TA+)} \\ i_1(t_1) &> 0 \text{ for S3 (TB+)} \\ i_1(t_2) &> 0 \text{ for S2 (TA-)} \\ i_1(t_3) &< 0 \text{ for S4 (TB-)} \end{aligned} \tag{55}$$

From figure 3-8, each interval can be identified (t_0, t_1, t_2, t_3, t_4). The steady state time domain analysis consists in modeling the series resonant inverter in a state space representation, where the primary current is a state variable. Therefore, the linear state equation can be defined as:

$$\dot{x}_{(t)} = A \cdot x_{(t)} + B \cdot V_{1k} \tag{56}$$

Where, $x_{(t)}$ is the state vector, A is the system matrix, B is the input matrix and V_{1k} is the output voltage of the inverter during interval k. Therefore:

$$x_{(t)} = \begin{pmatrix} i_1(t) \\ v_c(t) \end{pmatrix} \;\; ; \quad A = \begin{pmatrix} -\frac{R_{eq}}{L_1} & -\frac{1}{L_1} \\ \frac{1}{C_1} & 0 \end{pmatrix} \;\; ; \quad B = \begin{pmatrix} \frac{1}{L_1} \\ 0 \end{pmatrix} \tag{57}$$

The solution of the state equations in the configuration k can be expressed as:

$$x_{(t)} = e^{A \cdot (t-t_k)} \cdot x(t_k) + A^{-1}\left(e^{A \cdot (t-t_k)} - I\right)B \;\cdot\; V_{1k} \tag{58}$$

Where, $x(t_k)$ is the value of the state variables at the beginning of the interval k. Therefore, from equation 58, and considering that the values of the state variables are continuous between each interval, the following equation can be derived:

$$x(t_{k+1}) = e^{A \cdot \Delta_k} \cdot x(t_k) + A^{-1}(e^{A \cdot \Delta_k} - I)B \;\cdot\; V_{1k} \tag{59}$$

Where,

$$\Delta_k = t_{k+1} - t_k \tag{60}$$

Using equations 59 and 60, the following set of linear equations can be obtained:

$$x(t_1) = e^{A \cdot \Delta_0} \;\cdot x(t_0) + A^{-1}(e^{A \cdot \Delta_0} - I)B \;\cdot\; V_{10}$$

$$x(t_2) = e^{A \cdot \Delta_1} \;\cdot x(t_1) + A^{-1}(e^{A \cdot \Delta_1} - I)B \;\cdot\; V_{11}$$

$$x(t_3) = e^{A \cdot \Delta_2} \;\cdot x(t_2) + A^{-1}(e^{A \cdot \Delta_2} - I)B \;\cdot\; V_{12}$$

$$x(t_0) = e^{A \cdot \Delta_3} \;\cdot x(t_3) + A^{-1}(e^{A \cdot \Delta_3} - I)B \;\cdot\; V_{13} \tag{61}$$

From figures 3-8 and 3-10, the relations between the time intervals and the control angles can be defined as follows:

$$\Delta_0 = \frac{(\beta - \alpha_+)}{360^\circ} T$$

$$\Delta_1 = \frac{\alpha_+}{360^\circ} T$$

$$\Delta_2 = \frac{(360^\circ - \beta - \alpha_-)}{360^\circ} T$$

$$\Delta_3 = \frac{\alpha_-}{360°} T \tag{62}$$

Finally, the linear equations from equation 61, can be rewritten in a matrix form as follows:

$$\begin{pmatrix} -e^{A\cdot\Delta_0} & I & 0 & 0 \\ 0 & -e^{A\cdot\Delta_1} & I & 0 \\ 0 & 0 & -e^{A\cdot\Delta_2} & I \\ I & 0 & 0 & -e^{A\cdot\Delta_3} \end{pmatrix} \begin{pmatrix} x(t_0) \\ x(t_1) \\ x(t_2) \\ x(t_3) \end{pmatrix} = \begin{pmatrix} A^{-1}(e^{A\cdot\Delta_0} - I)B \cdot V_{10} \\ A^{-1}(e^{A\cdot\Delta_1} - I)B \cdot V_{11} \\ A^{-1}(e^{A\cdot\Delta_2} - I)B \cdot V_{12} \\ A^{-1}(e^{A\cdot\Delta_3} - I)B \cdot V_{13} \end{pmatrix} \tag{63}$$

Solving the matrix, will result in the solution of state vector x, in which the value of the state variable $I_1$is obtained for the beginning of each interval. With these values, the conditions stated in equation 55 can be verified in order to confirm the ZVS operation in each semiconductor.

3.5 Design and Simulation of a Series-series Compensated IPT System

In chapter 2, a SS IPT system was design and simulated with a signal generator. At the beginning of chapter 3, an appropriate power supply was selected for the system in order to transfer rated load power. Now, an optimum control strategy will be selected in order to regulate the voltage that will feed the IPTT applying soft switching techniques. For this, the three control strategies reviewed in this chapter will be simulated: PS, ADC and o_AVC control. The control strategy selected, will be the one that achieves ZVS in all semiconductors for the operation point of the system.

It is important to mention that an adjustment needs to be done in the value of the secondary capacitor that was design before. This is because now, the switching frequency (f_s) is higher than the resonant frequency (f_o), in order to satisfy the ZVS condition. Therefore, the following actions are proposed:

- The value of the secondary capacitor needs be calculated based on the switching frequency of the inverter (f_s). This will ensure resonance in the secondary coil.
- Verify for second time, if the selected normalized switching frequency is higher than the minimum normalized switching frequency to guarantee ZVS operation. This is because after making the adjustments, Q_1 will decrease, therefore increasing the minimum normalized switching frequency.

The following table summarizes the parameters and theoretical values of the SS compensated IPTT that were determined in chapter 2 and on the beginning of this chapter.

Table 3-1 Summary of the Values of the SS compensated IPTT

IPTT Parameters	
Element	**Value**
L_1	149.03 µH
L_2	23.26 µH
M	13.115 µH
R_1	0.298 Ω
R_2	0.1175 Ω
R_{ac}	1.3 Ω
k	0.223
Air Gap	25 mm
$f_o = f_s$	40 kHz
Capacitive Compensation	
Element	**Value**
C_2	680.63 nF
C_1(SS)	106.23 nF
Theoretical Values	
V_{dc}	18.2648 V
I_1	2.0667 A
$V_{1(1)}$	16.441 V
I_2	4.8038 A
P_{ac}	30 W
η	88.28 %
Q_1	4.7073
Q_2	4.1241

Based on these values, and using equation 50 and 54, it is possible to determine the initial minimum normalized switching frequency of the system for each control strategy. The results are plotted in figure 3-13.

It can be seen in figure 3-13, as expected, that o_AVC is the only control strategy that maintains a minimum normalized switching frequency, achieving ZVS operation while regulating the output voltage of the inverter. From the figure, the normalized switching frequency (ω_n) is selected to be 1.04. Therefore, f_o= 40 kHz and f_s= 41.6 kHz.

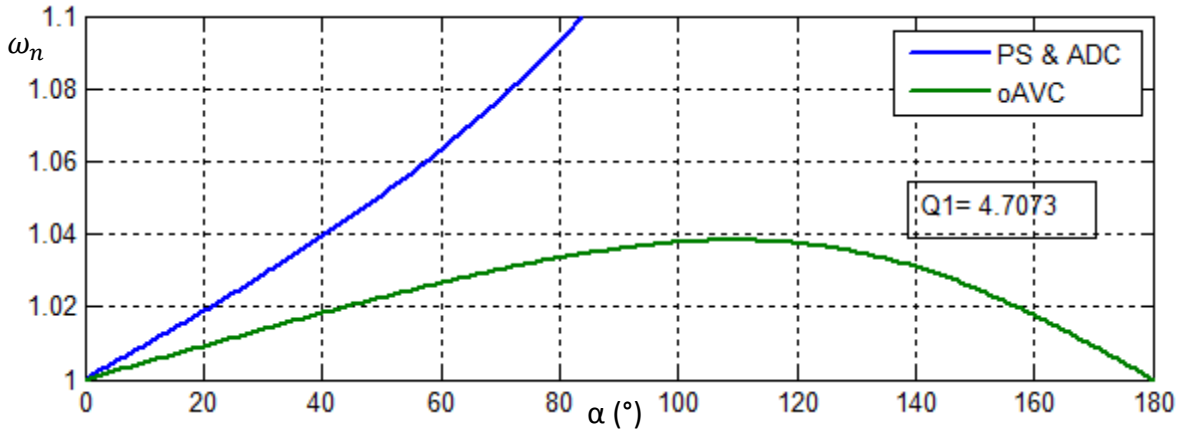

Fig. 3-13 Initial minimum normalized switching frequency (ω_n) for ZVS

As mentioned on the actions proposed in page 50, the value of the secondary capacitor will be modified. Resulting in C_2= 629.28 nF using equation 9. The value of the primary capacitor will remain the same.

With this new value of f_s, the new primary loaded quality factor will be Q_1= 4.5391 using equation 32. Therefore, also following the second action proposed in page 50, the minimum normalized switching frequency is verified for a second time, giving the following final plot.

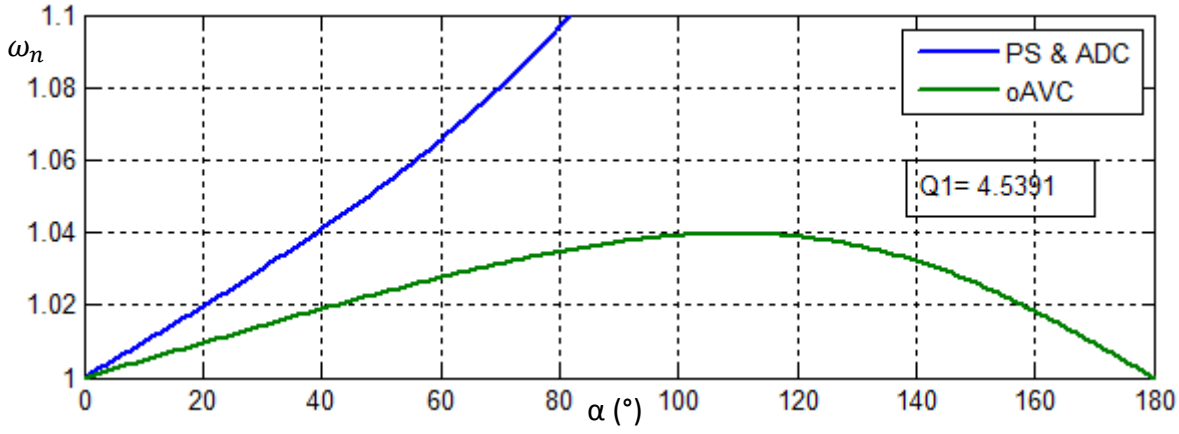

Fig. 3-14 Final minimum normalized switching frequency (ω_n) for ZVS

It can be seen in figure 3-14, that for a normalized switching frequency of 1.04, ZVS operation will still be achieve for o_AVC control strategy.

Continuing to the next step of the design, the DC link voltage will be fixed at 25 V. Therefore, using equations 47 and 51, it is possible to determine the value of α for each control strategy in order to obtain the required output voltage in the inverter. The results are as follows:

- For PS and ADC control: $\alpha = 73.5751°$
- For o_AVC control: $\alpha = 87.4966°$

From figure 3-14, it can be seen that at $\alpha = 73.5751°$ for PS and ADC control, the normalized switching frequency needs to be around 1.08 in order to maintain ZVS operation. On the other hand, with o_AVC control, with a normalized switching frequency of 1.04, ZVS operation will be maintain for any value of α between 0° and 180°.

Furthermore in the design, the ZVS verification technique that was reviewed in section 3.4, will be implemented in order to verify the ZVS operation in each control strategy at a normalized switching frequency of 1.04.

Solving the matrix of equation 63 and comparing the values with the conditions of equation 55, will give the following results:

- For PS control:

$i_1(t_0) = 0.786$ A (No ZVS)
$i_1(t_1) = 2.3933$ A (ZVS)
$i_1(t_2) = -0.7860$ A (No ZVS)
$i_1(t_3) = -2.3933$ A (ZVS)

- For ADC control:

$i_1(t_0) = 0.4805$ A (No ZVS)
$i_1(t_1) = 2.6808$ A (ZVS)
$i_1(t_2) = 2.6808$ A (ZVS)
$i_1(t_3) = 0.4805$ A (No ZVS)

- For o_AVC control:

$i_1(t_0) = -0.3422$ A (ZVS)

$i_1(t_1) = 3.0013$ A (ZVS)

$i_1(t_2) = 0.0323$ A (ZVS)

$i_1(t_3) = -0.3422$ A (ZVS)

Table 3-2 Summary of the Values of the SS IPT System with o_AVC control

IPTT Parameters	
Element	**Value**
L_1	149.03 µH
L_2	23.26 µH
M	13.115 µH
R_1	0.298 Ω
R_2	0.1175 Ω
R_{ac}	1.3 Ω
k	0.223
Air Gap	25 mm
f_o (for C_1)	40 kHz
f_s (for C_2)	41.6 kHz
ω_n	1.04
Capacitive Compensation	
Element	**Value**
C_2	629.28 nF
C_1(SS)	106.23 nF
Theoretical Values	
V_{dc}	25 V
I_1	1.9872 A
$V_{1(1)}$	18.0257 V
I_2	4.8038 A
P_{ac}	30 W
η	88.53 %
Q_1	4.5391
Q_2	4.2890

Figures 3-15, 3-16 and 3-17 show the simulation waveforms results of the circuit in figure 3-2 using the three control strategies. Additional, table 3-2 shows the analytical results using the

equations reviewed before. Here, the theoretical and simulation results are validated. Concluding that o_AVC strategy is the best option to regulate the power flow of the system.

Figure 3-19 shows the final simulation waveforms of the SS compensated IPTT being regulated by the fixed frequency o_AVC control, achieving ZVS operation in all semiconductors of the inverter. As can be seen, the theoretical values stated in table 3-2 match really well with the simulation results.

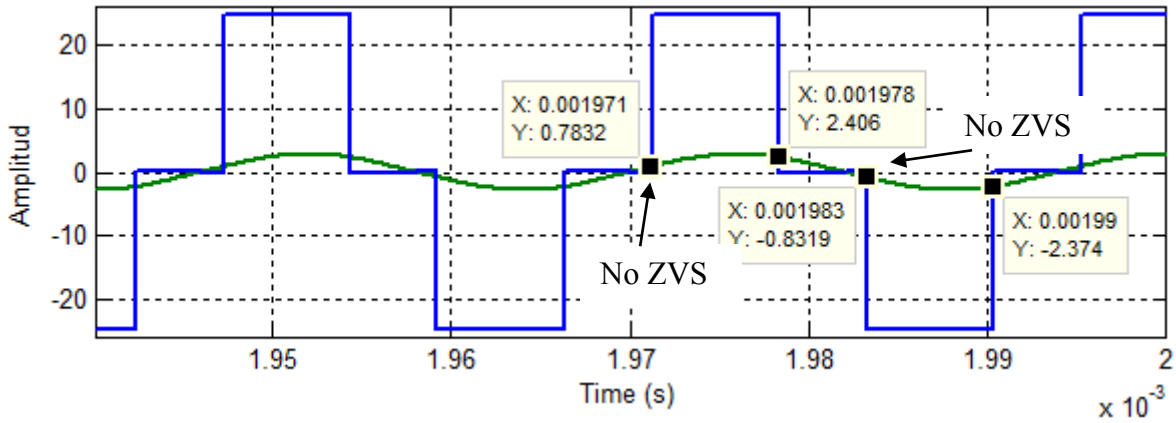

Fig. 3-15 Verification of ZVS in PS control

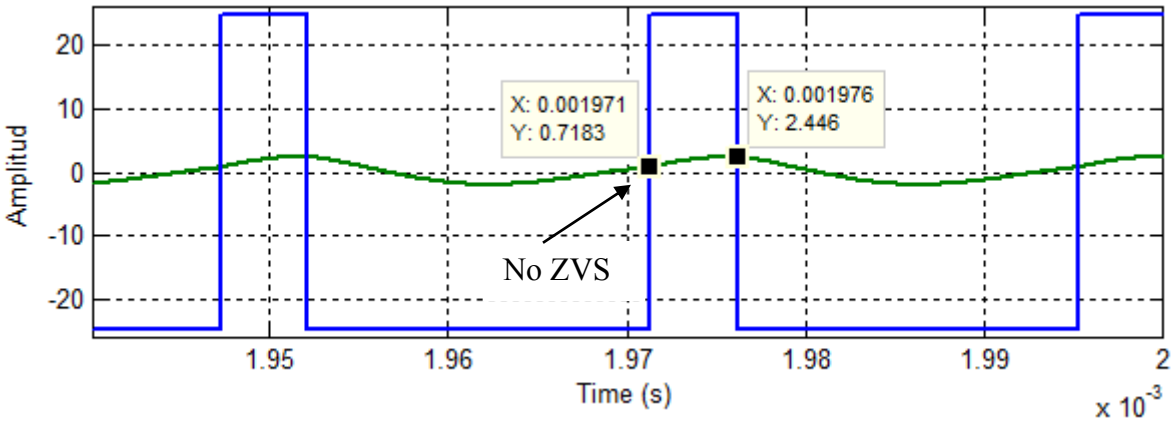

Fig. 3-16 Verification of ZVS in ADC control

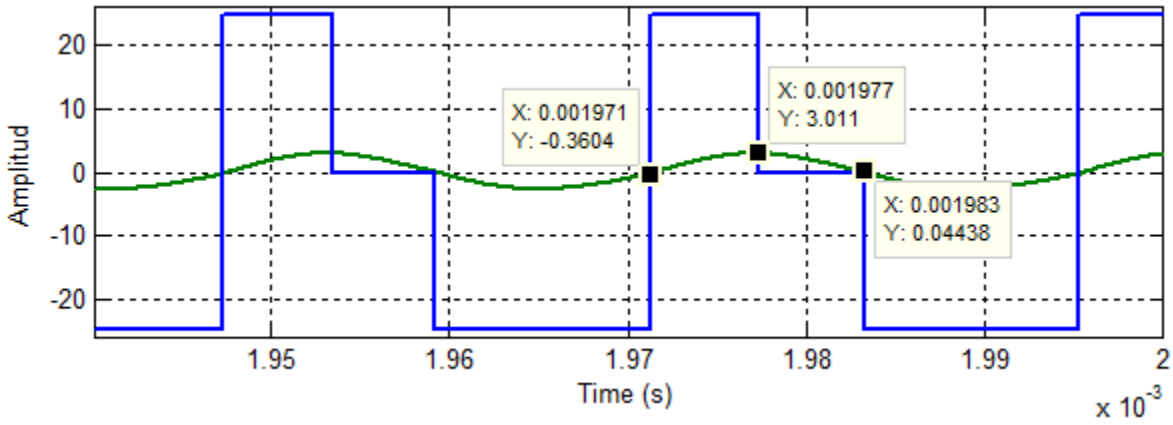

Fig. 3-17 Verification of ZVS in o_AVC control

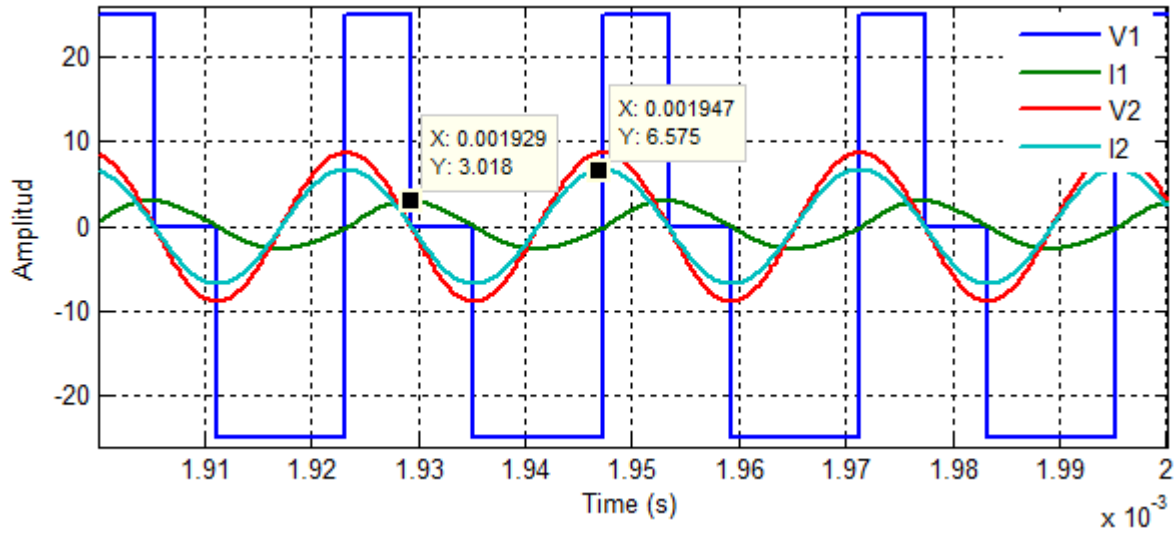

Fig. 3-18 Final simulation waveforms of the SS compensated IPTT with o_AVC control

3.6 Summary

In this chapter, the concept of power supply in IPT systems was explained. The analysis of operation for a full bridge series resonant inverter was presented and applied to the SS compensated IPT system reviewed in chapter 2. Initial simulation waveforms operating at resonant frequency ($f_s = f_o$) were presented, showing successful results. Additionally, a fixed frequency optimum control strategy (o_AVC control) was studied in order to achieve ZVS operation while controlling the power flow of the system (operation at minimum normalized switching frequency). A detailed analysis was made for this control strategy demonstrating through mathematical procedures its advantages compared to conventional control strategies (PS and ADC control). Finally, a ZVS verification technique was presented in order to verify analytically the conditions to achieve soft switching (ZVS).

All the studies reviewed in the chapter were applied to the SS compensated IPTT design in chapter 2; obtaining satisfactory results between the analytical calculations and simulation waveforms.

In conclusion, the equations derived were validated giving precise results, the o_AVC control technique showed to be more efficient for the SS compensated IPTT compared to the PS and ADC control, and finally, the ZVS verification technique was implemented satisfactory suiting perfectly for IPT applications.

CHAPTER 4

EXPERIMENTAL SETUP AND TEST RESULTS

4.1 Introduction

As it was mentioned before, the main goal of this work is to study de fundamentals of IPT systems in order to design an IPTT and study its power transfer capabilities. Many analysis and theoretical calculations were implemented obtaining satisfactory simulation results.

In this stage of the study, an experimental setup is intended to be built in order to validate the design theory and simulation results. For this, the objective of this chapter will be design and build a pulse generator capable to satisfy the characteristics of the proposed control strategy (o_AVC) and also operate at the required switching frequencies. Additionally, build an IPTT system (coils and compensation circuits) based on the design characteristics to validate the equations derived in chapter 2. And finally, demonstrate the effectiveness of the ZVS verification strategy explained in chapter 3.

With the experimental setup and test results, the theory explained in the previous chapters can be validated. This will show the effectiveness of the analytical calculations applied to this design.

4.2 Pulse Generator

As it was reviewed, the SS compensated IPTT that was design is feed by a full bridge inverter. The output voltage of the inverter can be regulated to half of its rated value by using the o_AVC control strategy. Therefore, it is important to design and build a device capable to generate pulses that meets the characteristics of this control strategy. As shown in figure 3-11, the following figure

will illustrate more in detail the waveforms of the pulses in each semiconductor for o_AVC control strategy.

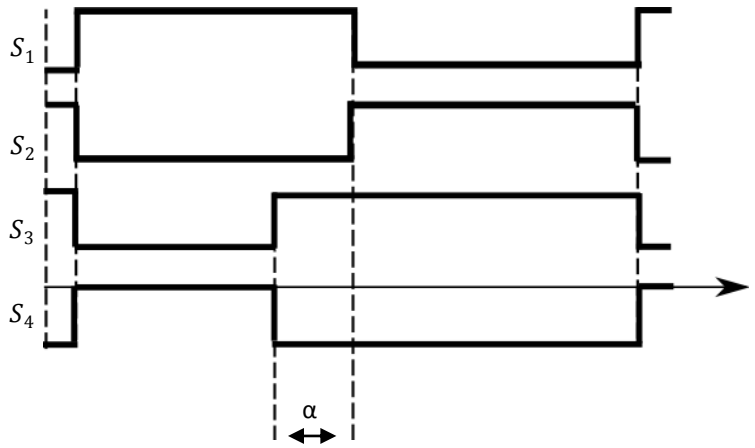

Fig. 4-1 Waveforms of the pulses for o_AVC control strategy

It can be seen in the figure, that if α is equal to zero, all the pulses will have a duty cycle of 0.5. It is important to remember that S_1 and S_2 corresponds to the leg A of the full bridge inverter, and in the same way S_3 and S_4 corresponds to leg B of the full bridge inverter.

The logic used in simulation was intended to be implemented in practice using software interfaces like OPAL-RT and dSpace. However, some "overrun" problems were encountered because of limitations with the sampling time. The maximum frequency of the pulses that could be generated was 20 kHz and still the waveforms were not very smooth. Only 5 samples per cycle.

Because of these limitations, other alternatives needed to be found. The first step was to locate an application that did not depend on the sampling time of the software interfaces in order to execute a command. The PWM block (DS1103SL_DSP_PWM) that dSpace has in the library offers this advantage. Pulses can be generated to up to 5 MHz; additionally, it counts with four independent inputs, which suits perfectly with the logic of the o_AVC control. No software outputs

are available for this block. The following figure shows the dSpace board that was used, the PC desktop and the PWM block.

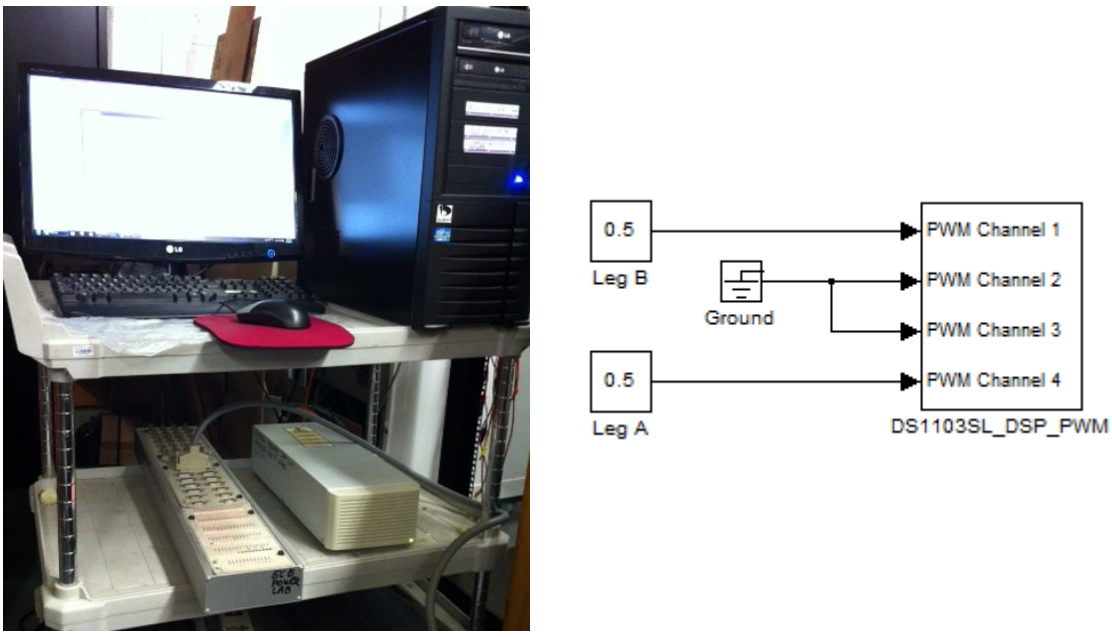

Fig. 4-2 dSpace board, PC desktop and PWM Block

At this point, the pulses for the semiconductors S_1 and S_4 can be generated with no problem, but now, these signals need to be inverter in order to have the other two pulses for semiconductors S_2 and S_3. Additionally, the digital outputs of the dSpace board (CP1103), gives signals of 5V. This could be a limitation for gate drivers in which pulse signals need to be higher than 5V.

Consequently, a simple and very effective solution was implemented. The use of a **SN7406 Hex Inverter Buffers/Drivers with Open-Collector High Voltage Outputs**. This device showed to operate very effectively for the requirements mentioned before. It inverts the input signals and is capable of amplifying the voltage of the output with the connection of a "pull up" resistor at the outputs. The following figures show the schematic of this device, the diagram of the circuit that

was implemented for each semiconductor and the setup that was finally built. For the experiment tests, “pull up” resistors of 1 kΩ were used and the voltage was amplified from 5V to 15V. It is important to mention that the pulse generator setup was built from scratch, purchasing the electronic components and using the laboratory tools.

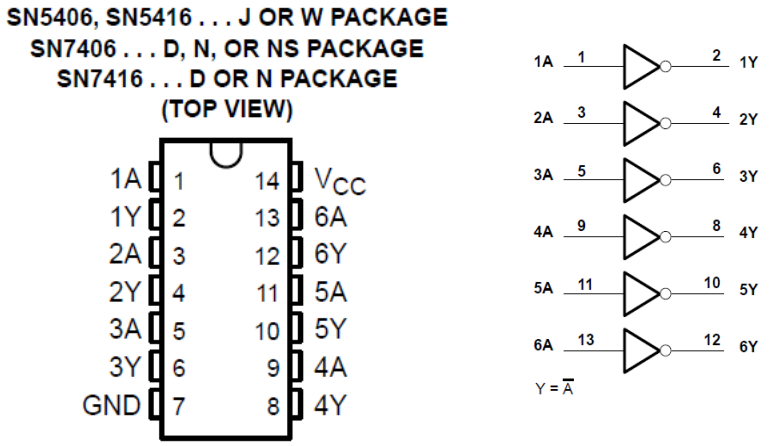

Fig. 4-3 Schematic and logic diagram of the SN7406 [32]

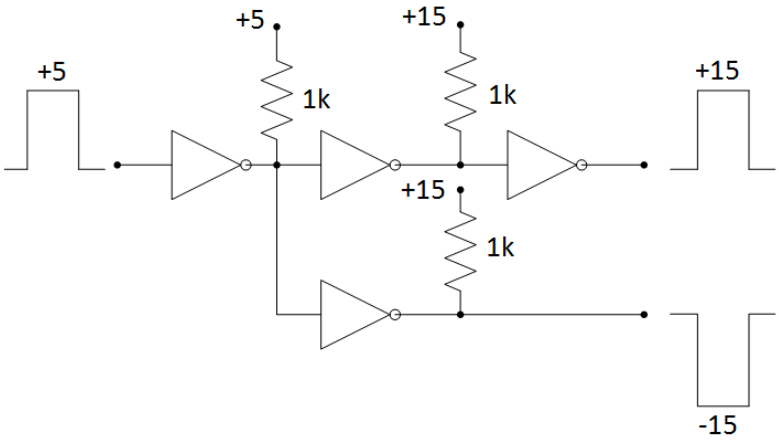

Fig. 4-4 Circuit diagram of the pulse generator for one leg of the inverter

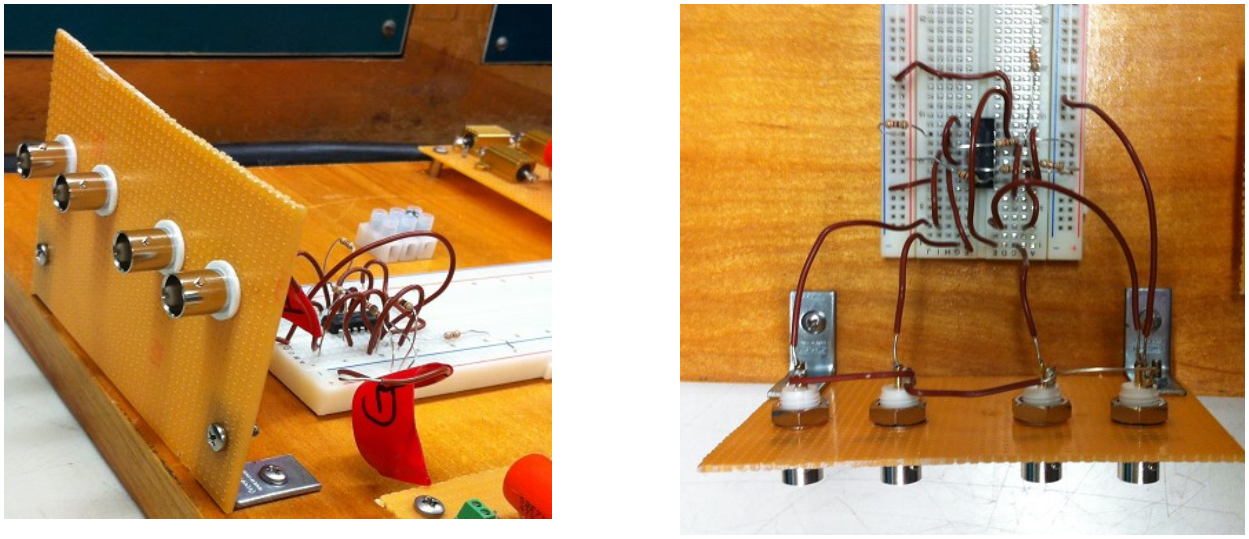

Fig. 4-5 Pulse generator setup

To test the pulse generator setup, pulses at 100 kHz were generated. First, for $\alpha = 0°$, and later for $\alpha = 90°$. The simulation waveforms were are also shown for comparison. Figures 4-6 and 4-7 show the results.

It can be seen in figures 4-6 and 4-7 that the o_AVC control strategy can be used effectively with the pulse generator setup that was built. In this case, the pulses have an amplitude of 15V as mentioned before. However, this value can be adjusted to other value higher than 5V. Additionally, the control logic was executed successfully. The test was made for a switching frequency of 100 kHz, to demonstrate that this setup can be used in other future designs.

Is important to mention, that the dead-time or blanking time is not being implemented in this setup. Therefore, this should be considered for inverters that do not have a blanking circuit generator. Otherwise, the inverter will short-circuit.

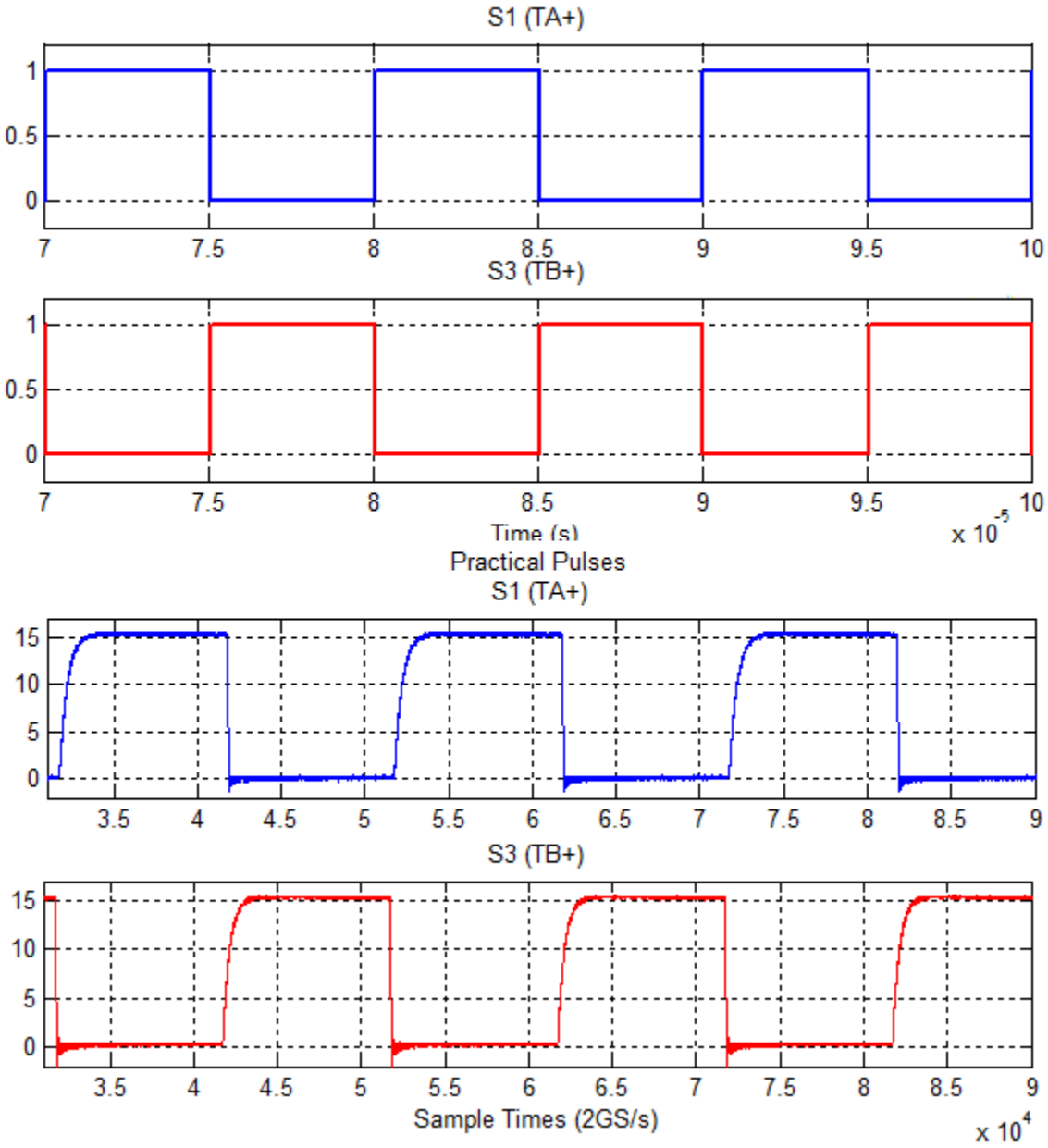

Fig. 4-6 Simulation and experimental setup pulses with α = 0°

Figure 4-6 compares the theoretical pulses with the experimental setup pulses obtained at 100 kHz. It is important to mention that only two semiconductors are shown because the other two are symmetrical. To verify the frequency from the practical waveforms, the sample time needs to be multiplied times $\frac{1}{2x10^9}$ to obtain a value in the time domain (s).

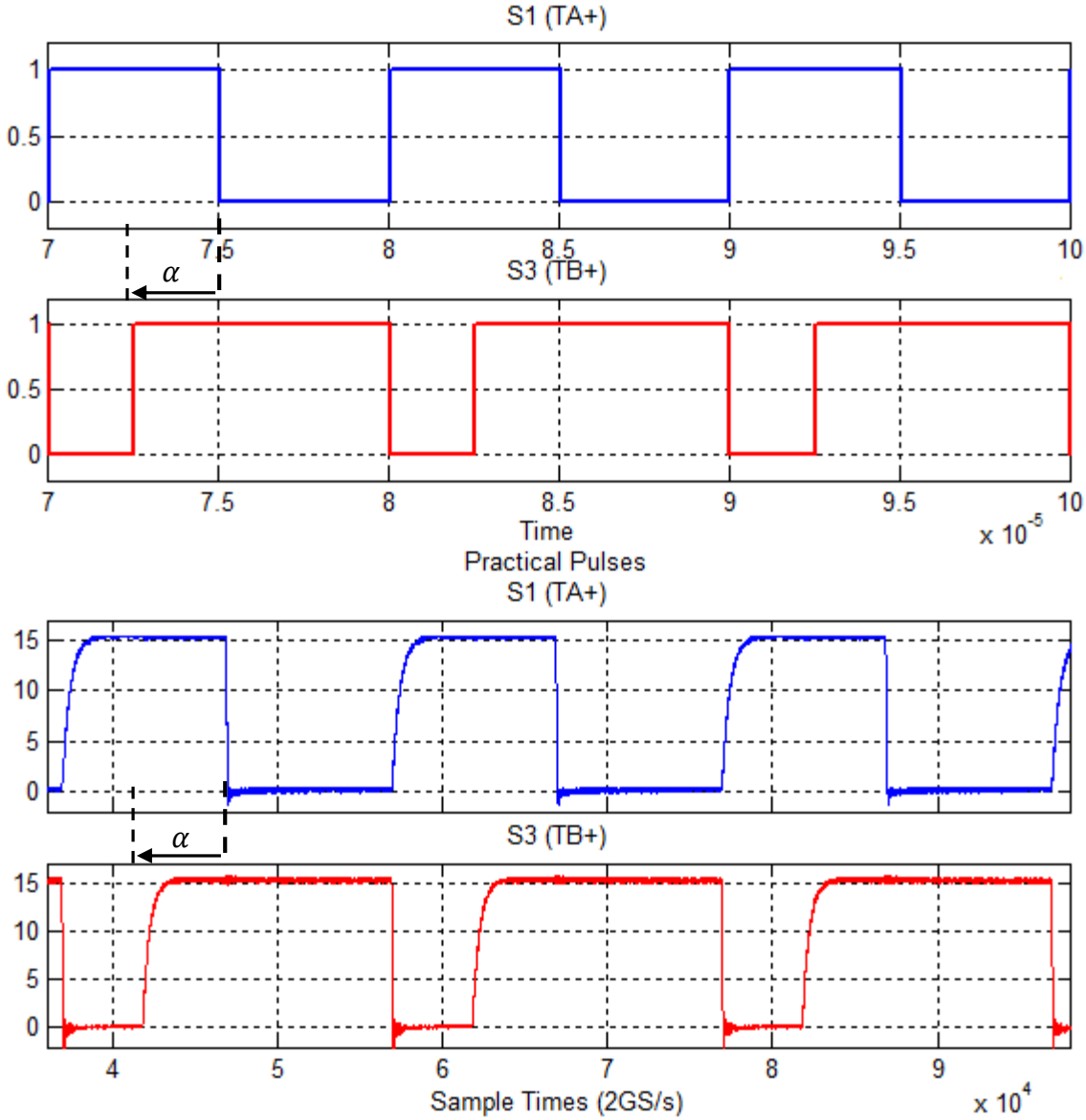

Fig. 4-7 Simulation and experimental setup pulses with $\alpha = 90°$

It can be seen in figure 4-7 how the pulse generator setup responds perfectly to the control strategy requirements. These waveforms can also be compared with figure 4-1.

A final implementation was achieved in the pulse generator. The intention of this final work was to facilitate the user interface with the pulse generator. A customized block, which calculates all the theoretical values of the IPT system was created in dSpace. Also, a user friendly

interface display was created in dSpace Control Desk developer, to control the pulse generator in real time and review the theoretical values calculated by the customized block. This will allow any user to control the power flow of the IPT system in real time and in a very simple and efficient way, and also know the theoretical values of the IPT system based on the input variables (P_{ac}, V_{dc}). The following figure shows the customized block and the user friendly interface display.

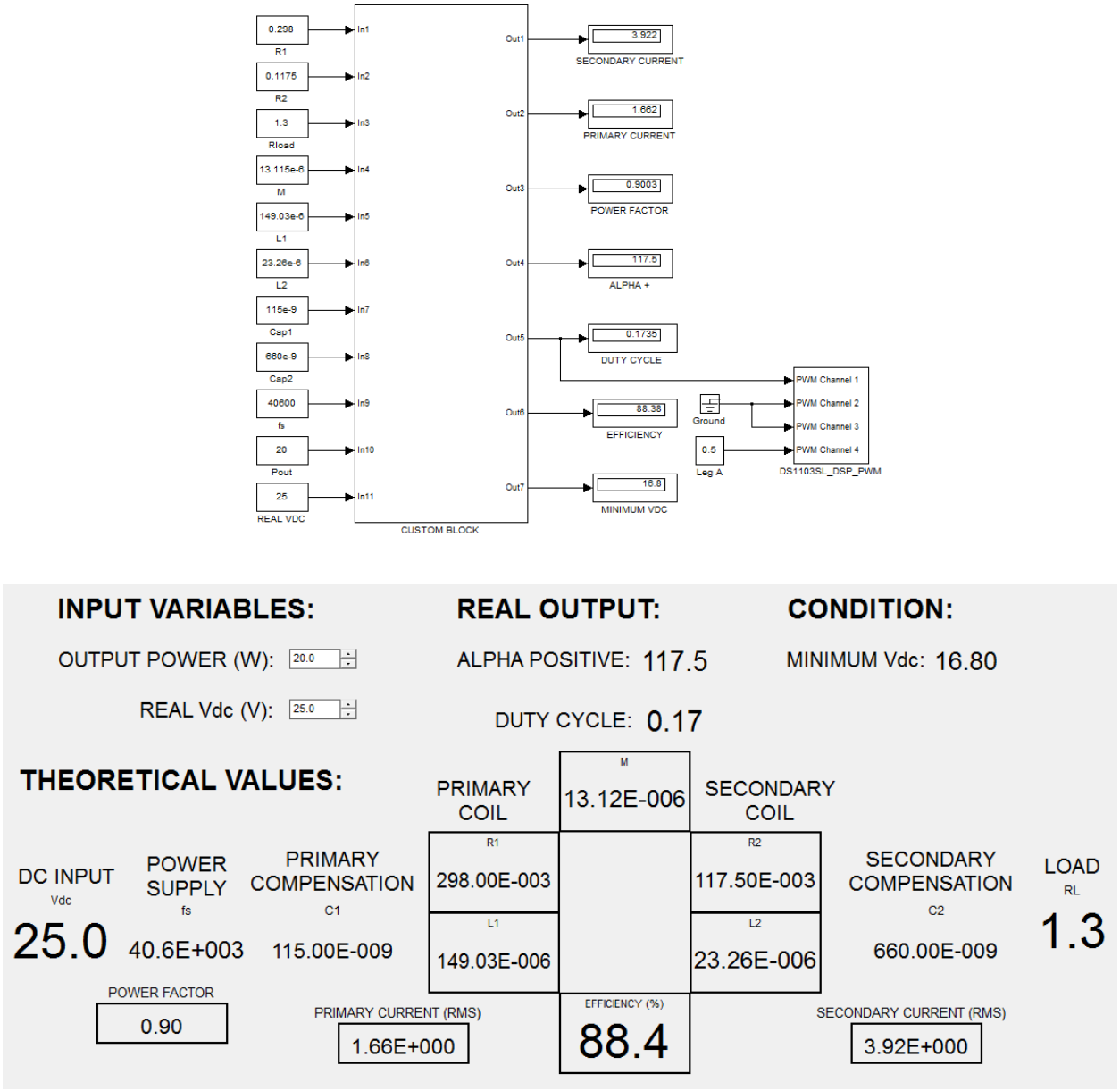

Fig. 4-8 Customized block and the user friendly interface display made in dSpace

4.3 Construction of the IPTT

4.3.1 Construction of the Coils

The following figure shows different coils designs that have been used in the literature review. This gave a good reference of how a simple IPTT design looks like.

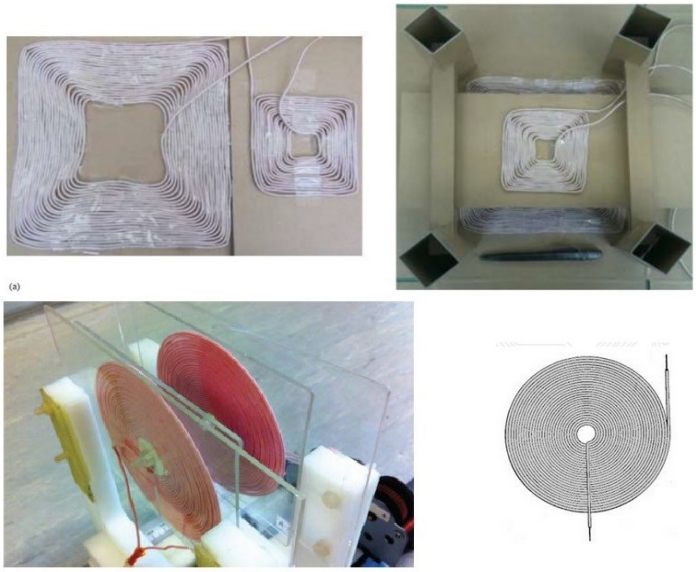

Fig. 4-9 Examples of coils design [9]-[33]

The type of wire used in the IPT, plays an important role on the systems performance. Because of the frequency of operation of the system, the skin effect increases the resistance of the windings affecting the efficiency. Therefore the most recommended type of wire to use is Litz Wire [34]-[35]-[36]. The wire that was purchased has the following specifications: Litz Wire 90/38 SPN SN (90 strans, 38 awg each strand). The wire is wrapped with a nylon textile for protection. Each coil winding was made by hand, giving the following characteristics:

Primary coil:

- Turns: 50
- Inner diameter: 1cm approx.
- Total diameter: 15cm approx.

Secondary coil:

- Turns: 25
- Inner diameter: 1cm approx.
- Total diameter: 7.5cm approx.

Figure 4-10 shows the final result of the primary and secondary coils construction. Also, figure 4-11 shows the coils setup using “standoffs” between them. The final air gap was measured to be 25 mm.

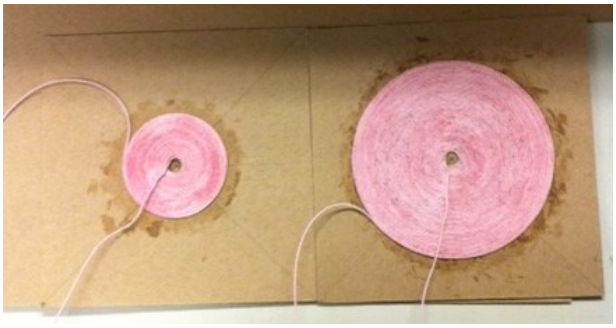

Fig. 4-10 Primary and secondary coil

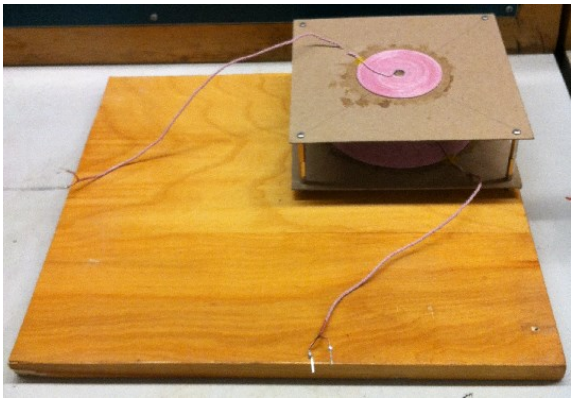

Fig. 4-11 Coils setup

4.3.2 COILS TERMINATION

Before terminating the tips of the coils, the insulation of each strand needs to me stripped or removed. This procedure is not that straight forward. A specific procedure needs to be followed in order to maximize the benefits of the litz wire.

An initial technique was followed using sand paper and later soldering the tips. See figure 4-12.

Fig. 4-12 Stripping strands insulation using sand paper

Later, the impedance analyzer available in the laboratory was used (HP 4194A), to measure the resistance and inductance of the coils in order to have a reference value. The results showed very inconsistent and high values for different frequencies. Therefore, a more efficient technique to remove the insulation from the tips of the coils had to be implemented. Figure 4-13 shows the impedance analyzer in operation.

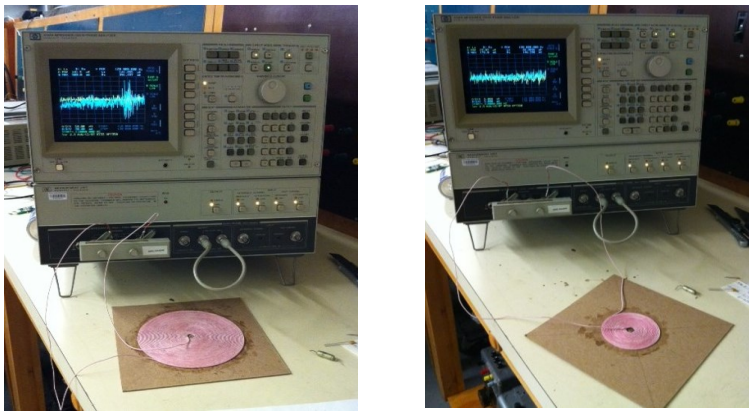

Fig. 4-13 Impedance analyzer HP 4194A in operation

The final method that was implemented was to dip the tips of the coils in sodium hydroxide using a solder pod. This procedure is recommended by NEMA MW 1000. See figure 4-14.

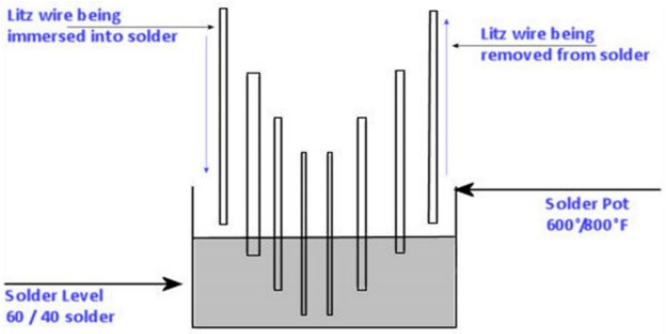

Fig. 4-14 Procedure to strip a litz wire using a solder pot [37]

4.3.2 RESISTANCE AND INDUCTANCE OF THE COILS

After terminating the coils, the internal resistance and inductance was measured. The following procedure was implemented.

Each coil was connected to a signal generator and the voltage and current waveforms were captured in order to measure the rms values and phase shift between them. Now, the resistance and self-inductance could easily be calculated by using the following equations:

$$| Z | = \frac{V_{rms}}{I_{rms}} \tag{64}$$

$$Z = R + j\omega L \tag{65}$$

Figure 4-15 shows how the primary coil was measured using a signal generator and oscilloscope. Figure 4-16 shows the measured waveforms.

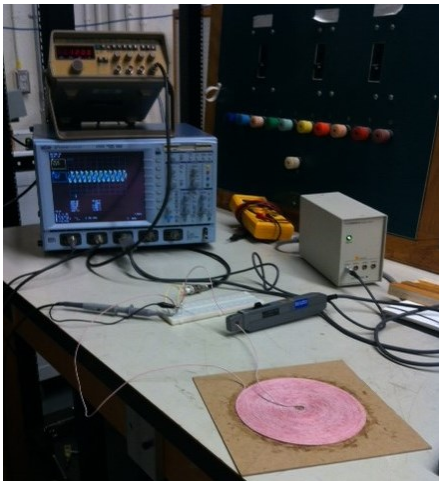

Fig. 4-15 Measurements in primary coil

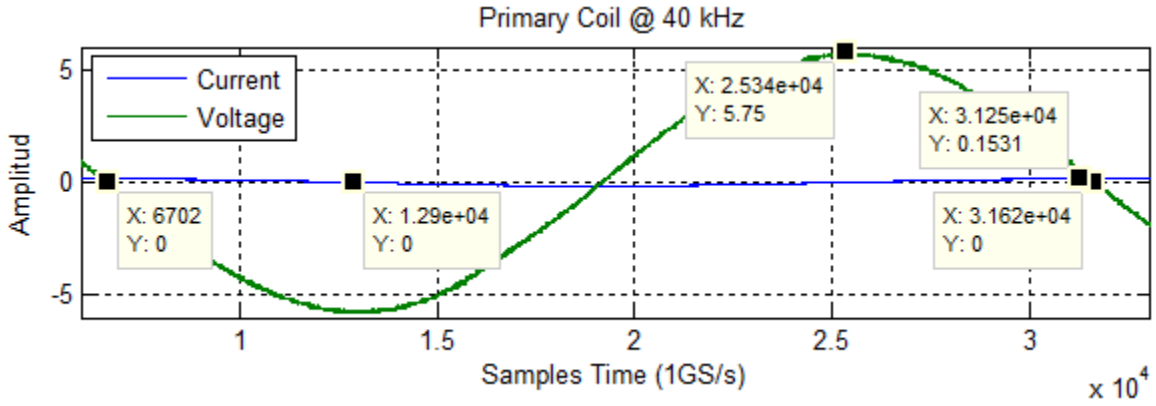

Fig. 4-16 Oscilloscope waveforms of measurements in primary coil

From figure 4-16, the following calculations can be made using equations 64 and 65:

$$t_1 = 6702 * 1x10^{-9} = 6.702\ \mu s$$

$$t_2 = 1.29x10^4 * 1x10^{-9} = 12.9\ \mu s$$

$$t_3 = 3.162x10^4 * 1x10^{-9} = 31.62\ \mu s$$

$$V_{rms} = \frac{5.75\ V}{\sqrt{2}} = 4.066\ V$$

$$I_{rms} = \frac{0.1531\ A}{\sqrt{2}} = 108.258\ mA$$

$$| Z | = \frac{4.066\ V}{108.258\ mA} = 37.56\ \Omega$$

$$\theta = \frac{(t_2 - t_1) * 360°}{t_3 - t_1} = 89.545°$$

$$Z = (0.298 + j37.558)\ \Omega$$

$$\omega L = 37.558$$

$$R_1 = 0.298\ \Omega, L_1 = 149.03\ \mu H$$

The same procedure will be implemented in the secondary coil. Figure 4-17 shows how the secondary coil was measured. Figure 4-18 shows the measured waveforms.

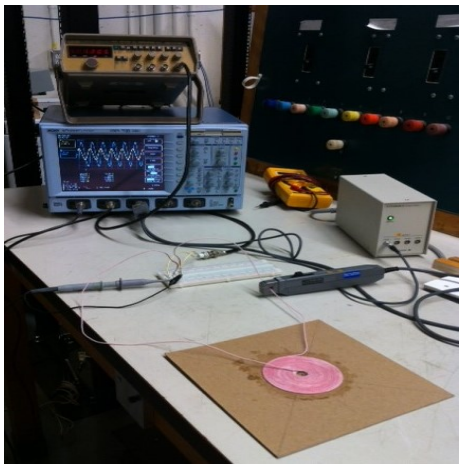

Fig. 4-17 Measurements in secondary coil

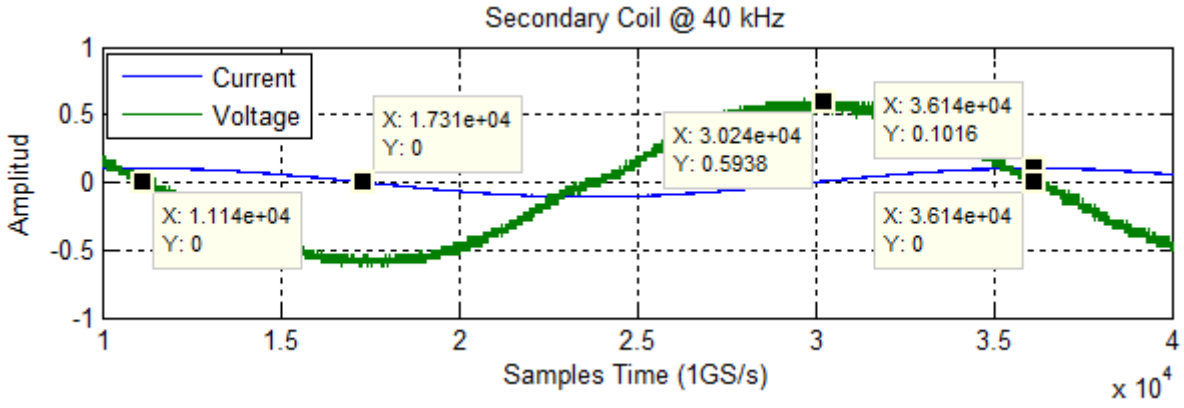

Fig. 4-18 Oscilloscope waveforms of measurements in secondary coil

In the same way as for the primary coil, from figure 4-18 using equation 64 and 65, the following calculations can be made:

$$t_1 = 1.114x10^4 * 1x10^{-9} = 11.14\ \mu s$$

$$t_2 = 1.731x10^4 * 1x10^{-9} = 17.31\ \mu s$$

$$t_3 = 3.614x10^4 * 1x10^{-9} = 36.14\ \mu s$$

$$V_{rms} = \frac{0.5938\ V}{\sqrt{2}} = 419.88\ mV$$

$$I_{rms} = \frac{0.1016\ A}{\sqrt{2}} = 71.84\ mA$$

$$|\ Z\ | = \frac{419.88\ mV}{71.84\ mA} = 5.845\ \Omega$$

$$\theta = \frac{(t_2 - t_1) * 360°}{t_3 - t_1} = 88.848°$$

$$Z = (0.1175 + j5.844)\ \Omega$$

$$\omega L = 5.844$$

$$R_2 = 0.1175\ \Omega, L_2 = 23.26\ \mu H$$

Now for the mutual inductance, both coils were positioned with the air gap support (25mm air gap). The primary coil was connected to the signal generator and the secondary coil was left open circuit. The oscilloscope was connected to capture and measure the primary current and the open circuit voltage of the secondary coil. The mutual inductance can now be calculated following equation (66). The derivation of this equation was mentioned in chapter 2 [38].

$$M = \frac{V_{oc}}{\omega I_1} \tag{66}$$

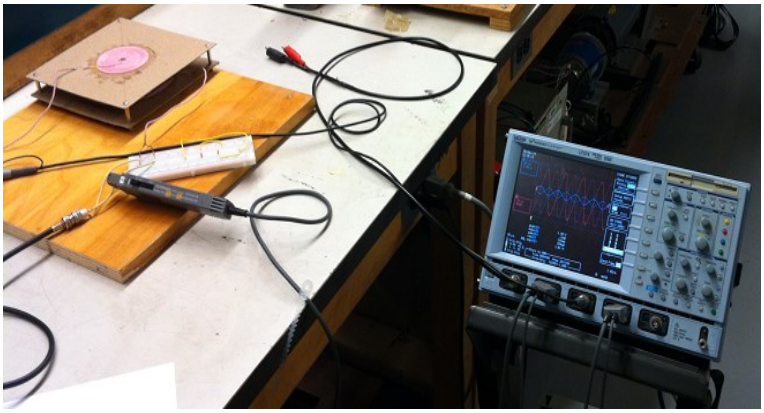

Fig. 4-19 Measurements of mutual inductance

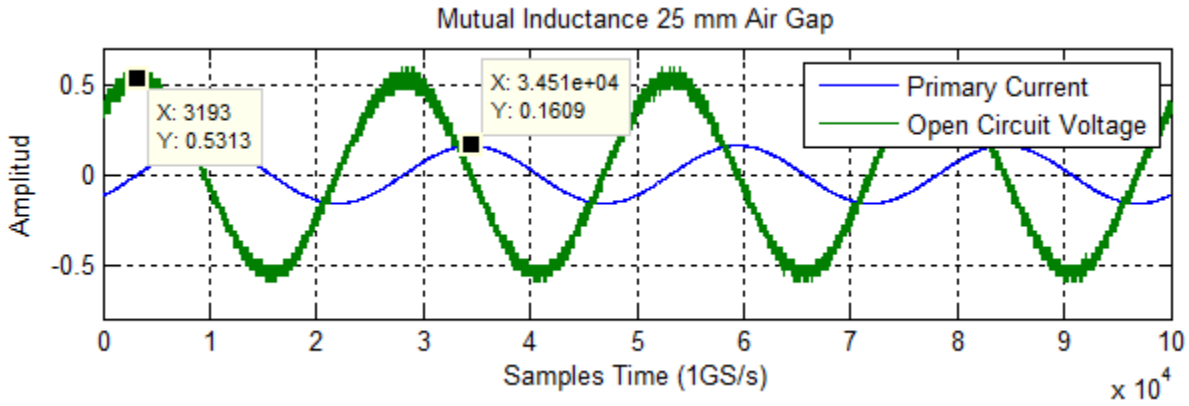

Fig. 4-20 Oscilloscope waveforms of measurements of mutual inductance

From figure 4-20 and equation 66, the mutual inductance of the coils can be calculated as follows:

$$M = \frac{\frac{0.5313}{\sqrt{2}}}{2\pi * 40.05x10^{3} * \frac{0.1609}{\sqrt{2}}} = 13.115\ \mu H \qquad (67)$$

It can be seen that the values obtained were the ones used in chapters 2 and 3, for the analytical analysis and calculations.

4.3.3 CONSTRUCTION OF CAPACITIVE COMPENSATION CIRCUIT BOARDS

As it was reviewed in table 3-2, the theoretical values of the capacitors for capacitive compensation are $C_1 = 106.23\ \text{nF}$ and $C_2 = 629.28\ \text{nF}$. However, because of practical availability, the values used for the setup are:

$$C_1 = 47\ \text{nF} + 68\ \text{nF} = 115\ \text{nF} \quad \text{(two capacitors)}$$

$$C_2 = 330\ \text{nF} + 330\ \text{nF} = 660\ \text{nF} \quad \text{(two capacitors)}$$

Two capacitive circuit boards were built; one for each coil. Additionally, the second board is composed by the resistive load. It is important to mention that these circuit boards were built from scratch, purchasing the required components and using the laboratory tools. Figure 4-21 shows the final result for the primary compensation circuit board and figure 4-22 shows the final experimental setup.

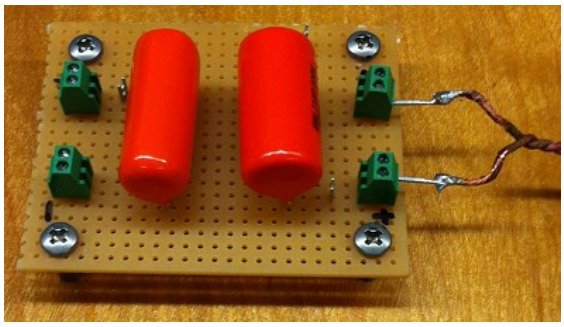

Fig. 4-21 Primary compensation circuit board

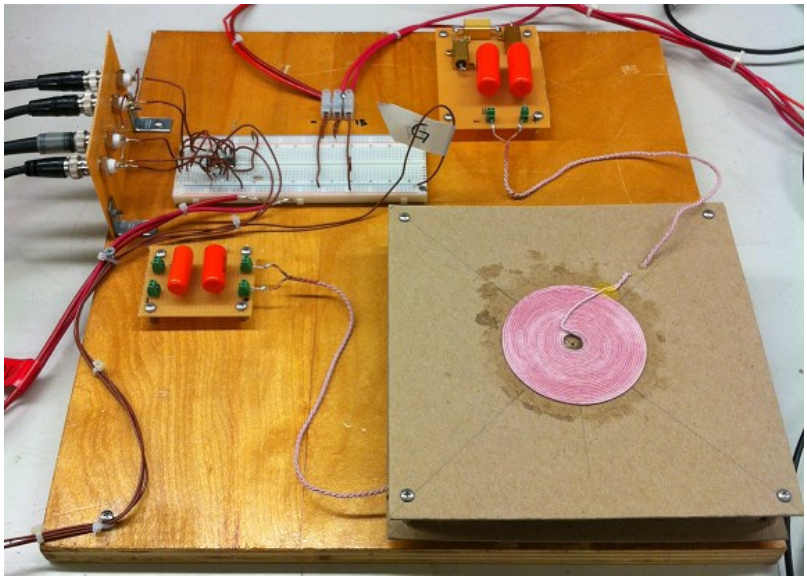

Fig. 4-22 Experimental Setup

4.3.4 PERFORMANCE VALIDATION

Based on the parameters obtained on the construction of the experimental setup. The following table summarizes the practical parameters of the system and the theoretical values. These results were obtained using the procedures explained in chapter 2 and 3.

To confirm the theoretical values, a comparison between simulation and experiment waveforms was performed. For the experiment test, a signal generator was used to supply a sinusoidal waveform of 40.6 kHz. The voltages and currents were measured with the oscilloscope. For the simulation, the same experimental setup parameters were used. The simulation and experimental waveforms are shown in figure 4-23.

Table 4-1 Practical parameters of the system and the theoretical values

Experimental Setup Parameters	
Element	**Value**
L_1	149.03 µH
L_2	23.26 µH
M	13.115 µH
R_1	0.298 Ω
R_2	0.1175 Ω
R_{ac}	1.3 Ω
k	0.223
Air Gap	25 mm
f_o (for C_1)	38.445 kHz
f_s (for C_2)	40.6 kHz
ω_n	1.056
Capacitive Compensation	
Element	**Value**
C_2	660 nF
C_1(SS)	115 nF
Theoretical Values	
V_s (signal generator)	7.07 V
I_1	0.1212 A
I_2	0.2860 A
η	88.38 %
Q_1	4.6394
Q_2	4.1859

It can be seen in figure 4-23, that the experiment waveforms match very well the simulation waveforms, giving a positive result for the design. This validates the measured values of the coils, mutual inductance and the calculated efficiency of the SS compensated IPTT.

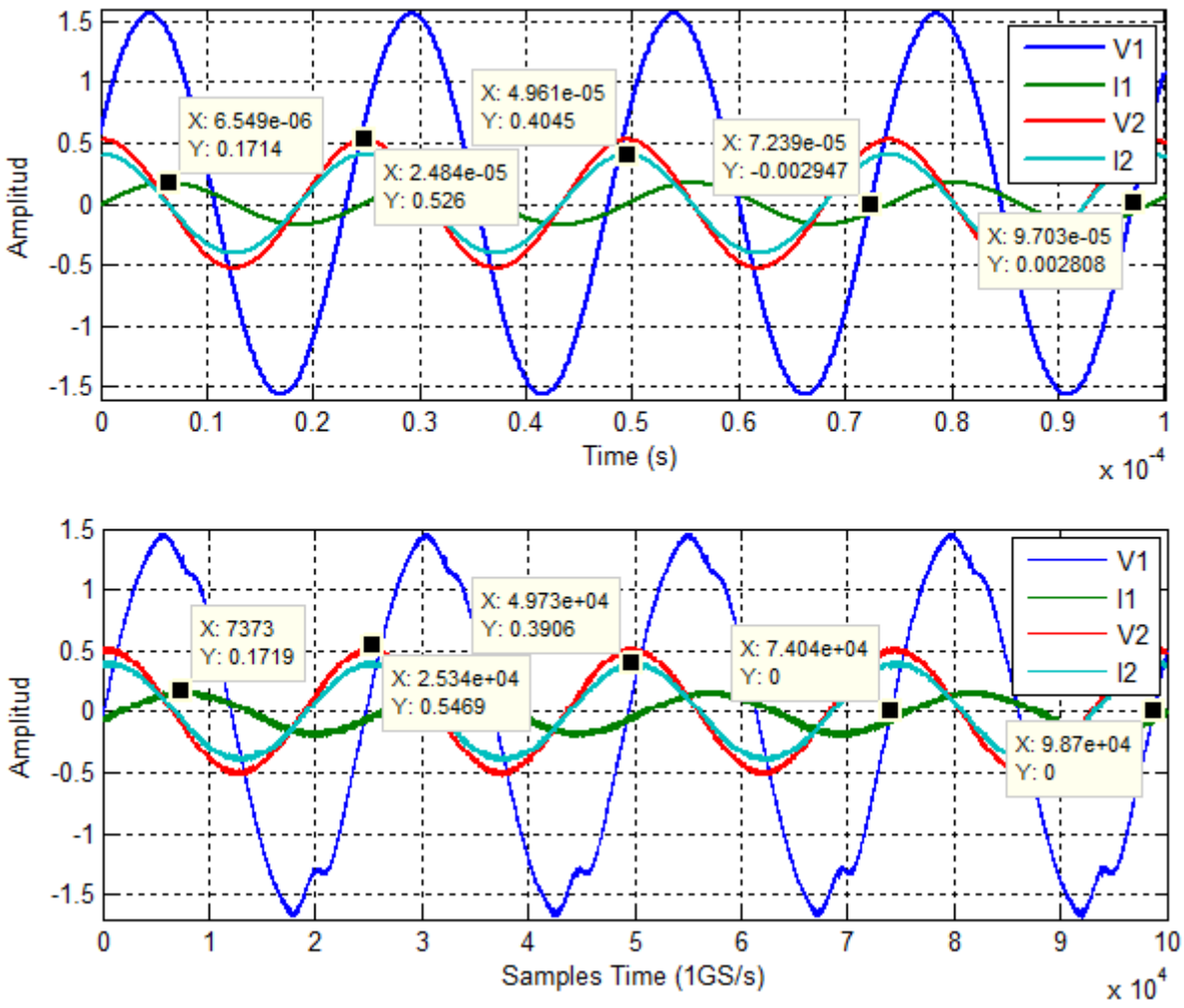

Fig. 4-23 Simulation and experimental waveforms

4.4 ZVS Verification

In this section, the ZVS verification technique reviewed in chapter 3 will be validated with the experimental results. It is already known that equation 55 states the condition to achieve ZVS operation. Solving the matrix of equation 63 for the values of the setup, the primary current in each interval resulted as follows:

$$i_1(t_0) = -0.0844 \text{ A}$$
$$i_1(t_1) = 0.0844 \text{ A}$$
$$i_1(t_2) = 0.0844 \text{ A}$$
$$i_1(t_3) = -0.0844 \text{ A}$$

Additionally, the following figure shows these values for the experimental waveforms.

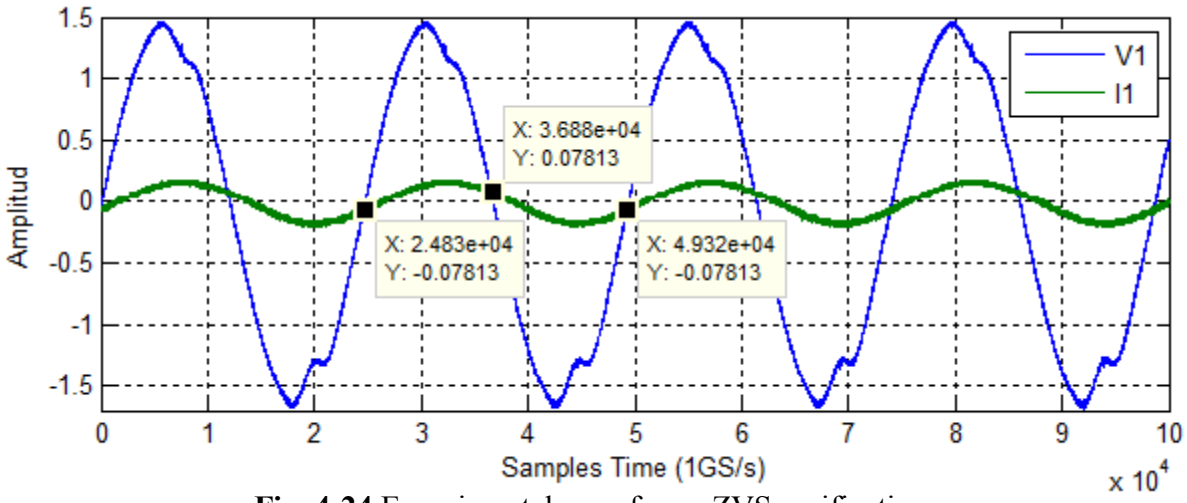

Fig. 4-24 Experimental waveforms ZVS verification

It can be seen in figure 4-24 that the experimental waveforms match with the theoretical results. Therefore, this strategy is a good approach to determine analytically if the ZVS condition is satisfied in the IPT power supply.

4.5 Summary

In this chapter, experimental results were presented in order to validate the theory reviewed in the previous chapters. First, a pulse generator was built using dSpace and a Hex inverter. Practical results were presented and compared to simulation waveforms. The test was performed at 100 kHz first with α = 0° and after with α = 90°. The results matched perfectly, confirming the correct operation of the pulse generator for this kind of applications. Additionally a customized block was generated in dSpace Control Desk developer, to obtain the theoretical values of the system based

on the input parameters. Also, a user friendly interface display was created to control the power flow in real time. These last implementations will facilitate the users operation in future works.

Additionally, an IPTT was built and mounted in a setup for practical tests. The parameters of the coils were measure trough proposed techniques and validated with the test results, which were compared with the theoretical calculations. The final results and waveforms matched perfectly, validating the measured techniques that were implemented.

Finally, the ZVS verification technique was validated with the practical waveforms obtained for the system, giving very precise results. This confirms that this technique can be applied to IPT systems.

CHAPTER 5

CONCLUSIONS AND FUTURE WORK

5.1 Summary

As it was mentioned in chapter 1, the idea of transferring electrical power through the air has existed since the 1900's with Nikola Tesla. However, many challenges remained for decades, making it difficult to succeed. One of the main limitations was the technology available for the time. Therefore, studies regarding this idea were considered not viable. However, since the end of the twentieth century, more interest started to develop, thanks to the technological improvements throughout time and the evolution of society's life style.

Important advances in power electronics have made this initial idea to become a reality. Now, it will depend on how much research and development it is carried out on this topic in order to make it more attractive, affordable, efficient and safe to general population. The future vision, is to make a positive impact in humanity and change the way electricity has been seen since its creation: through wires. This is why studies and research in IPT technology is so important nowadays.

This thesis focused in studying two important elements of an IPT system: the power supply and the resonant circuit. An IPT system was designed using the theory reviewed and considerations proposed. Finally, an experimental setup was built to validate the theoretical calculations and estimations. More specifically, the following conclusions can be made:

1) Successful validation of the IPT theory reviewed in chapter 2 with the simulation results, giving the exact same values for a SS compensation IPTT. This topology was selected because of advantages that were identified for this study. The optimal operation point

strategy and tuning and resonant considerations that were proposed were also validated, showing satisfactory results in the simulation: 88.3% of efficiency and a sinusoidal primary current. These results covers the resonant circuit stage.

2) Effective confirmation of the concepts reviewed in chapter 3, for the power supply and control strategies, with simulation results giving the exact same values as analytical calculations. An optimum control strategy to reduce the switching losses was identified and compared with the conventional control strategies. The advantages of the optimum control strategy were demonstrated by simulation, giving satisfactory results. Additionally, a ZVS verification technique was also identified and implemented in the analysis in order to guarantee a higher performance of the system. The simulation results matched perfectly with the analytical calculations.
3) Creation of a pulse generator setup using dSpace and a Hex Inverter, giving successful results at 100 kHz testing the optimum control strategy that was proposed (o_AVC). Additionally, a customized block and user friendly interface display was created in order to analyze and implement practical tests more easily the SS compensated IPTT setup or any future design.
4) Construction of an experimental setup for the SS compensated IPTT, which showed successful results compared to the theoretical calculations. In this way, the practical methodology that was implemented to obtain the parameters of the coils was also validated.

In conclusion, an IPT system was modeled, simulated and practically tested giving a power transfer efficiency of 88.38%, as expected, though a 25mm air gap. A fixed frequency control strategy was proposed for the power supply to guarantee ZVS operation. Additionally, design

methodologies and advanced mathematical techniques were studied and implemented in the modeling giving satisfactory results.

5.2 Potential Future Work

Over the course of this investigation, numerous opportunities were found in order to give a continuity to this work and take the most of the setup that was built in future studies. These future work opportunities are described as follows:

1) Construction of a full bridge resonant inverter using low-voltage power MOSFETS to be connected and tested to the pulse generator and SS compensated IPTT setup. The idea is to perform the test using the control strategy proposed in this thesis.
2) Construction of a rectifier considering the characteristics of the IPT system setup. The power flow can also be regulated in this stage of the system [39]. A practical comparison can be made in order to determined which method will be more beneficial.
3) Analyze the parameters of the IPTT by using a finite element analysis software [40]. For examples ANSYS. This will allow a more detail analysis regarding the coupling behavior between the coils for different designs, distances, etc.
4) Controller design for the IPT system setup by varying the distance between the coils [41]. This will lead to a variation in the value of the mutual inductance (M) which will affect the specifications of the system.

REFERENCES

[1] Zhang Bingyi; Liu Hongbin; Zhao Yisong; Ying Yong; Feng Guihong, "Contactless electrical energy transmission system using separable transformer," *Electrical Machines and Systems, 2005. ICEMS 2005. Proceedings of the Eighth International Conference on* , vol.3, no., pp.1721,1724 Vol. 3, 29-29 Sept. 2005

[2] Qingxin Yang; Jiangui Li; Haiyan Chen; Junhua Wang, "Design and analysis of new detachable coreless transformer used for contact-less electrical energy transmission system," *Vehicle Power and Propulsion Conference, 2008. VPPC '08. IEEE* , vol., no., pp.1,4, 3-5 Sept. 2008

[3] Chwei-Sen Wang; Stielau, O.H.; Covic, G.A., "Design considerations for a contactless electric vehicle battery charger," *Industrial Electronics, IEEE Transactions on* , vol.52, no.5, pp.1308,1314, Oct. 2005

[4] Bossche, Alex Van Den., and Vencislav Valchev. “Inductors and Transformers for Power Electronics”. Boca Raton: Taylor & Francis, 2005. Print

[5] Green, A. W.; Boys, J. T., "10 kHz inductively coupled power transfer-concept and control," *Power Electronics and Variable-Speed Drives, 1994. Fifth International Conference on* , vol., no., pp.694,699, 26-28 Oct 1994

[6] Stielau, O.H.; Covic, G. A., "Design of loosely coupled inductive power transfer systems," *Power System Technology, 2000. Proceedings. PowerCon 2000. International Conference on* , vol.1, no., pp.85,90 vol.1, 2000

[7] Covic, G.A.; Boys, J.T., "Inductive Power Transfer," *Proceedings of the IEEE* , vol.101, no.6, pp.1276,1289, June 2013

[8] Elliott, G. A J; Boys, J.T.; Green, A. W., "Magnetically coupled systems for power transfer to electric vehicles," *Power Electronics and Drive Systems, 1995., Proceedings of 1995 International Conference on* , vol., no., pp.797,801 vol.2, 21-24 Feb 1995

[9] Chopra, S.; Bauer, P., "Analysis and design considerations for a contactless power transfer system," *Telecommunications Energy Conference (INTELEC), 2011 IEEE 33rd International* , vol., no., pp.1,6, 9-13 Oct. 2011

[10] Chopra, S.; Prasanth, V.; Mansouri, B.E.; Bauer, P., "A contactless power transfer — Supercapacitor based system for EV application," *IECON 2012 - 38th Annual Conference on IEEE Industrial Electronics Society* , vol., no., pp.2860,2865, 25-28 Oct. 2012

[11] Chwei-Sen Wang; Covic, G.A.; Stielau, O.H., "General stability criterions for zero phase angle controlled loosely coupled inductive power transfer systems," *Industrial Electronics Society, 2001. IECON '01. The 27th Annual Conference of the IEEE* , vol.2, no., pp.1049,1054 vol.2, 2001

[12] Chwei-Sen Wang; Covic, G.A.; Stielau, O.H., "General stability criterions for zero phase angle controlled loosely coupled inductive power transfer systems," *Industrial Electronics Society, 2001. IECON '01. The 27th Annual Conference of the IEEE* , vol.2, no., pp.1049,1054 vol.2, 2001

[13] Chwei-Sen Wang; Stielau, O.H.; Covic, G.A., "Load models and their application in the design of loosely coupled inductive power transfer systems," *Power System Technology, 2000. Proceedings. PowerCon 2000. International Conference on* , vol.2, no., pp.1053,1058 vol.2, 2000

[14] Boys, J. T.; Covic, G. A.; Green, A. W., "Stability and control of inductively coupled power transfer systems," *Electric Power Applications, IEE Proceedings* - , vol.147, no.1, pp.37,43, Jan 2000

[15] Kazimierczuk, Marian, and Dariusz Czarkowski. “Resonant Power Converters”. New York: Wiley, 1995. Print

[16] Mohan, Ned, Tore M. Undeland, and William P. Robbins. “Power Electronics: Converters, Applications, and Design”. Hoboken, NJ: John Wiley & Sons, 2003. Print

[17] Chwei-Sen Wang; Covic, G.A.; Stielau, O.H., "Power transfer capability and bifurcation phenomena of loosely coupled inductive power transfer systems," *Industrial Electronics, IEEE Transactions on* , vol.51, no.1, pp.148,157, Feb. 2004

[18] Sanzhong Bai; Pantic, Z.; Lukic, S., "A comparison study of control strategies for ZVS resonant converters," *IECON 2010 - 36th Annual Conference on IEEE Industrial Electronics Society* , vol., no., pp.256,262, 7-10 Nov. 2010

[19] Burdío, J.M.; Barragan, L.A.; Monterde, F.; Navarro, D.; Acero, J., "Asymmetrical voltage-cancellation control for full-bridge series resonant inverters," *Power Electronics, IEEE Transactions on* , vol.19, no.2, pp.461,469, March 2004

[20] Chen Duan; Chenguang Jiang; Taylor, A.; Bai, K., "Design of a zero-voltage-switching large-air-gap wireless charger with low electrical stress for Plugin Hybrid Electric Vehicles," *Transportation Electrification Conference and Expo (ITEC), 2013 IEEE* , vol., no., pp.1,5, 16-19 June 2013

[21] Kazimierczuk, M.K.; Czarkowski, D., "Phase control of series resonant converter," *Power Electronics Specialists Conference, 1993. PESC '93 Record., 24th Annual IEEE* , vol., no., pp.1002,1008, 20-24 Jun 1993

[22] Hayes, J. G.; Mohan, N.; Henze, C.P., "Zero-voltage switching in a constant frequency digitally controller resonant DC-DC power converter," *Applied Power Electronics Conference and Exposition, 1988. APEC '88. Conference Proceedings 1988., Third Annual IEEE* , vol., no., pp.360,367, 1-5 Feb 1988

[23] Kazimierczuk, M.K.; Jutty, M.K., "Fixed-frequency phase-controlled full-bridge resonant converter with a series load," *Power Electronics, IEEE Transactions on* , vol.10, no.1, pp.9,18, Jan 1995

[24] Borage, M.B.; Nagesh, K. V.; Bhatia, M.S.; Tiwari, S., "Characteristics and Design of an Asymmetrical Duty-Cycle-Controlled LCL-T Resonant Converter," *Power Electronics, IEEE Transactions on* , vol.24, no.10, pp.2268,2275, Oct. 2009

[25] Burdio, J.-M.; Canales, F.; Barbosa, P.M.; Lee, F.C., "Comparison study of fixed-frequency control strategies for ZVS DC/DC series resonant converters," *Power Electronics Specialists Conference, 2001. PESC. 2001 IEEE 32nd Annual* , vol.1, no., pp.427,432 vol. 1, 2001

[26] Barragan, L.A.; Burdío, J.M.; Artigas, J.I.; Navarro, D.; Acero, J.; Puyal, D., "Efficiency optimization in ZVS series resonant inverters with asymmetrical voltage-cancellation control," *Power Electronics, IEEE Transactions on* , vol.20, no.5, pp.1036,1044, Sept. 2005

[27] Sharp, B.; Wu, H., "Asymmetrical Voltage-Cancellation control for LCL resonant converters in Inductive Power Transfer systems," *Applied Power Electronics Conference and Exposition (APEC), 2012 Twenty-Seventh Annual IEEE* , vol., no., pp.661,666, 5-9 Feb. 2012

[28] Imbertson, P.; Mohan, N., "Asymmetrical duty cycle permits zero switching loss in PWM circuits with no conduction loss penalty," *Industry Applications Society Annual Meeting, 1991., Conference Record of the 1991 IEEE* , vol., no., pp.1061,1066 vol.1, Sept. 28 1991-Oct. 4 1991

[29] Imbertson, P.; Mohan, N., "New directions in DC-DC power conversion based on idealized concepts leading ultimately to the asymmetrical duty-cycle power converter," *Circuits and Systems I: Fundamental Theory and Applications, IEEE Transactions on* , vol.44, no.8, pp.722,727, Aug 1997

[30] Hosseini, S.H.; Goharrizi, A.Y., "Harmonic Optimization of Asymmetrical Voltage-Cancellation Control for Full-Bridge Series Resonant Inverters," *SICE-ICASE, 2006. International Joint Conference* , vol., no., pp.4350,4353, 18-21 Oct. 2006

[31] Monterde, F.; Burdío, J.M.; Hernandez, P.; Garcia, J.R., "Unipolar voltage-cancellation control of resonant inverters for induction cooking appliances," *Industrial Electronics Society, 1998. IECON '98. Proceedings of the 24th Annual Conference of the IEEE* , vol.2, no., pp.820,824 vol.2, 31 Aug-4 Sep 1998

[32] Texas Instrument. "SN5406, SN5416, SN7406, SN7416 HEX INVERTER BUFFERS/DRIVERS WITH OPEN-COLLECTOR HIGH-VOLTAGE OUTPUTS". Dallas: Texas Instrument, 1983. Print.

[33] Wei Zhang; Siu-Chung Wong; Tse, C.K.; Qianhong Chen, "Design for Efficiency Optimization and Voltage Controllability of Series–Series Compensated Inductive Power Transfer Systems,"*Power Electronics, IEEE Transactions on* , vol.29, no.1, pp.191,200, Jan. 2014

[34] Sallan, J.; Villa, J.L.; Llombart, A.; Sanz, J.F., "Optimal Design of ICPT Systems Applied to Electric Vehicle Battery Charge," *Industrial Electronics, IEEE Transactions on* , vol.56, no.6, pp.2140,2149, June 2009

[35] Villa, J.L.; Llombart, A.; Sanz, J.F.; Sallan, J., "Practical Development of a 5 kW ICPT System SS Compensated with a Large Air gap," *Industrial Electronics, 2007. ISIE 2007. IEEE International Symposium on* , vol., no., pp.1219,1223, 4-7 June 2007

[36] Covic, G.A.; Boys, J.T., "Modern Trends in Inductive Power Transfer for Transportation Applications," *Emerging and Selected Topics in Power Electronics, IEEE Journal of* , vol.1, no.1, pp.28,41, March 2013

[37] HM Wire International Inc. "Soldering of Litz Wire". Ohio: HM Wire International, 2007. Print.

[38] Covic, G.A.; Kissin, M.L.G.; Kacprzak, D.; Clausen, N.; Hao Hao, "A bipolar primary pad topology for EV stationary charging and highway power by inductive coupling," *Energy Conversion Congress and Exposition (ECCE), 2011 IEEE* , vol., no., pp.1832,1838, 17-22 Sept. 2011

[39] Keeling, N.A.; Covic, G.A.; Boys, J.T., "A Unity-Power-Factor IPT Pickup for High-Power Applications," *Industrial Electronics, IEEE Transactions on* , vol.57, no.2, pp.744,751, Feb. 2010

[40] Cong Zheng; Rui Chen; Faraci, E.; Zahid, Z.U.; Senesky, M.; Anderson, D.; Jih-Sheng Lai; Wensong Yu; Chien-Yu Lin, "High efficiency contactless power transfer system for

electric vehicle battery charging," *Energy Conversion Congress and Exposition (ECCE), 2013 IEEE* , vol., no., pp.3243,3249, 15-19 Sept. 2013

[41] Wu, H.H.; Gilchrist, A.; Sealy, K.D.; Bronson, D., "A High Efficiency 5 kW Inductive Charger for EVs Using Dual Side Control," *Industrial Informatics, IEEE Transactions on* , vol.8, no.3, pp.585,595, Aug. 2012

[42] Peschiera, B.; Williamson, S.S., "Review of inductive power transfer technology for electric and plug-in hybrid electric vehicles," *Industrial Electronics Society, IECON 2013 - 39th Annual Conference of the IEEE* , vol., no., pp.4672,4677, 10-13 Nov. 2013

[43] Peschiera, B.; Williamson, S.S., "Review and comparison of inductive charging power electronic converter topologies for electric and plug-in hybrid electric vehicles," *Transportation Electrification Conference and Expo (ITEC), 2013 IEEE* , vol., no., pp.1,6, 16-19 June 2013

[44] Lukic, S.; Pantic, Z., "Cutting the Cord: Static and Dynamic Inductive Wireless Charging of Electric Vehicles," *Electrification Magazine, IEEE* , vol.1, no.1, pp.57,64, Sept. 2013